National Aeronautics and Space Administration

Shallow Subsurface Structures of Volcanic Fissures

Principal Investigator: Carolyn Parcheta (3223)

Jeremy Nash (347H), Catherine Pavlov (Caltech), Kalind Carpenter (347B), Nick Wiltsie (347C), Aaron Parness (347C), Karl Mitchell (3223)

Introduction

Fig 1. 2011 fissure eruption of Kilauea Volcano, Hawai'i. Photo courtesy of USGS.

Volcanic fissure vents (Fig 1) are difficult to quantify. Obtaining data has been Impossible because fissures are:

- too thin for geophysical methods
- buried by eruption deposits

Researchers and modelers assume a first-order (planar) feature, but ***is this correct*** *at magmatic scales* (i.e., individual lava fountains)?

Hypothesis*: Fissures conduits are* ***NOT*** *vertical or parallel-walled*

Originality

We have developed a robot, VolcanoBot (Fig 2), to acquire the first, robust, and diagnostic data of eruptive fissure conduit geometries.

Fig 2. VolcanoBot descending a fake rock wall.

Importance

The surface geometric expression of fissures is quantified through roughness, irregularity, and sinuosity (Parcheta et al., 2015, Fig 2). This project and data set:

- integrates state-of-the-art robotics and computer vision with the frontiers of volcano science
- is first-of-it's-kind for volcanic conduits.
- compares surface and sub-surface geometries to eruption style
- provides a framework for understanding planetary eruptions

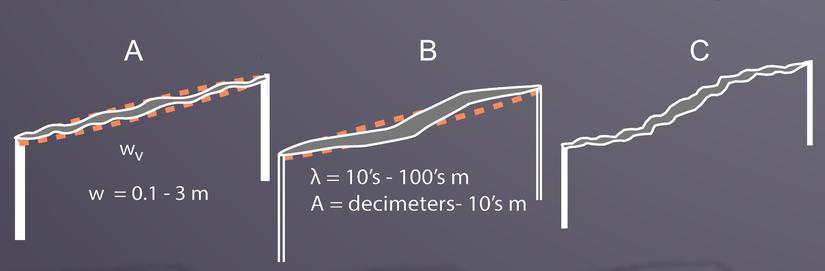

Fig 3. A: irregularity is the change of vent width from a planar geometry.
B: Sinuosity is the change in vent direction from a planar geometry.
C: Reality has both feautures superimposed on each other.

Acknowledgements

This work is funded by a *NASA Postdoctoral Fellowship* through **Oak Ridge Associated Universities** and took place at:

National Aeronautics and Space Administration
Jet Propulsion Laboratory
California Institute of Technology
Pasadena, California

www.nasa.gov

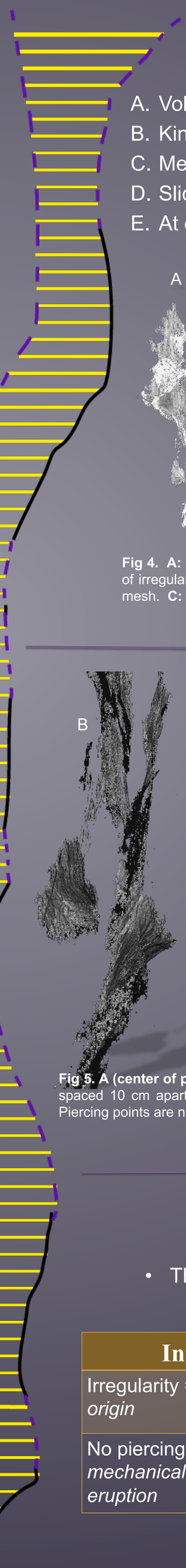

Methodology

A. VolcanoBot measures the geometry in NIR structured light
B. Kinect Fusion Large Scale processes Raw IR data
C. Mesh output (Fig 4a) is sliced in Meshlab
D. Slices (Fig 4b, 4c) produce our measurement grid (Fig 4d)
E. At each10 cm grid node, we measure conduit width

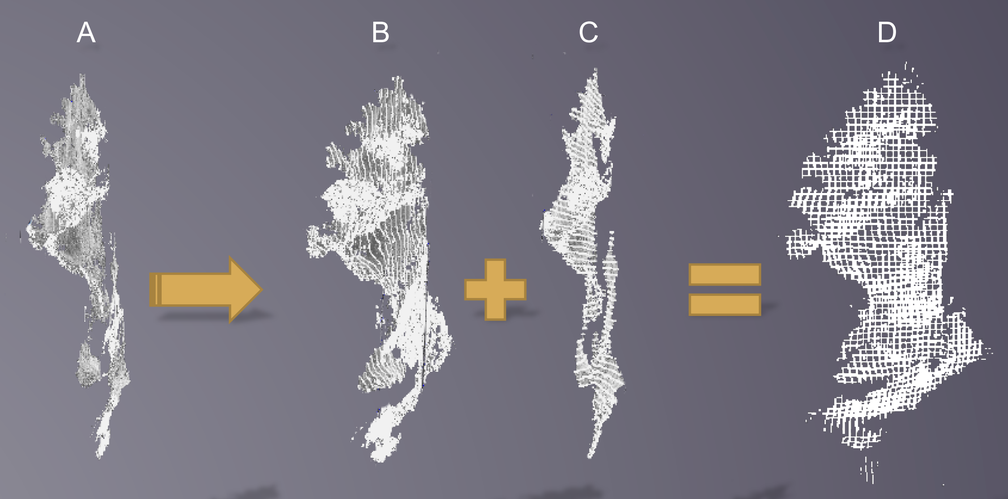

Fig 4. A: Mesh output of Kinect Fusion. Gaps in the mesh are data holes on the underside of irregularities (a result of our downward viewing angle). **B:** Vertical slices contouring the mesh. **C:** Horizontal slices contouring the mesh. **D:** measurement grid produced by slices.

Preliminary Results

1. Shallow subsurface (<13 m deep) irregularities are 30-50 cm wide, 1-2 m long similar to surface pattern
2. Some piercing points match across the fissure walls (Fig 5a), but some areas appear eroded (Fig 5b)
3. The conduit has 50 cm width variation (30 – 80 cm)
4. The conduit shifts south by 98 cm!
5. Fissure dips predominantly south, but also north!

Fig 5. A (center of poster): Piercing points are present. Yellow lines are width measurements, spaced 10 cm apart. Solid black walls indicate data, Purple dashed walls are inferred. **B:** Piercing points are not present. Image is a textured mesh surface.

Discussion

- The initial data supports our hypothesis that fissures are NOT planar features on magmatic scales.

Interpretation	Impact
Irregularity = *fracture mechanics origin*	Fissures and earthquake faults propagate the same way.
No piercing points = *walls mechanically eroded during eruption*	Fluid dynamics may not be passive. Induced turbulence? Supersonic foam?

Poster No. EA -1

National Aeronautics and Space Administration

Heterogeneous Deformation During the 2010 Mw 7.2 El Mayor-Cucapah Earthquake from Geodetic Data

Principal Investigator: Mong-Han Huang (329-A)
Eric J. Fielding (329-A)

The 4th of April 2010 *Mw* 7.2 El Mayor-Cucapah (EMC) earthquake in Baja California and Sonora, Mexico has primarily right-lateral strike-slip motion and minor north slip component. The surface rupture extends about 120 km west of the plate boundary between the Pacific Plate and the North American Plate. The EMC event initiated at the center, and ruptured bilaterally into an east-dipping strike-slip fault system to the north and a west-dipping strike-slip system in the south. In addition, geophysical evidences indicate high lateral heterogeneity from the Pacific Peninsular in the west to east of the Salton Trough. Here we use geodetic measurements including GPS, InSAR (SAR interferometry), and sub-pixel offset measurements to characterize the fault slip system during the EMC event. We optimize fault geometry as well as sub-fault slip distribution based on geodetic measurements. With considering homogeneous or layered earth structures, we find that the choice of earth structure could vary coseismic slip by 1.6 m, about 60% slip of deep slip. Additionally, we could further improve geodetic data fitting by considering change of crustal thickness as well as elastic moduli in different tectonic blocks. Our results imply that consideration of layered earth structure and lateral heterogeneity is necessary for calculating slip amplitude and distribution, which is crucial when estimating viscoelastic relaxation or stress-driven afterslip during the postseismic period.

Study Area

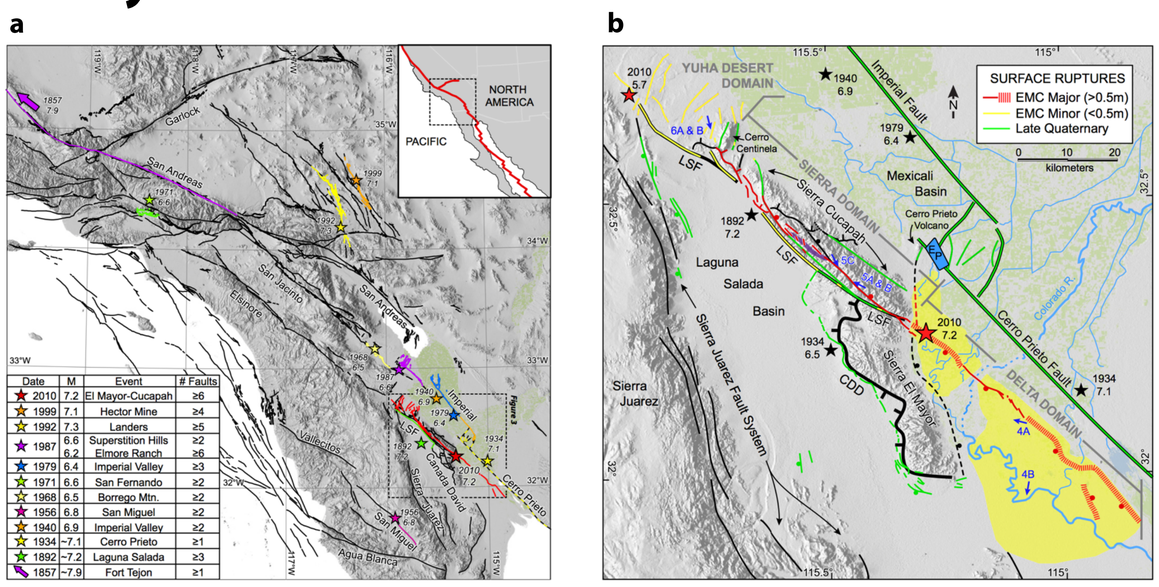

(a) Tectonic map of study area (after Fletcher et al., 2014). The black lines are mapped fault traces. The colored lines and stars represent historical events, and the red lines are the 2010 EMC surface rupture. **(b)** Close-up of the EMC event. The red start near Sierra El mayor shows the earthquake epicenter, and this event ruptured at least 6 discrete faults.

Moho depth (km)

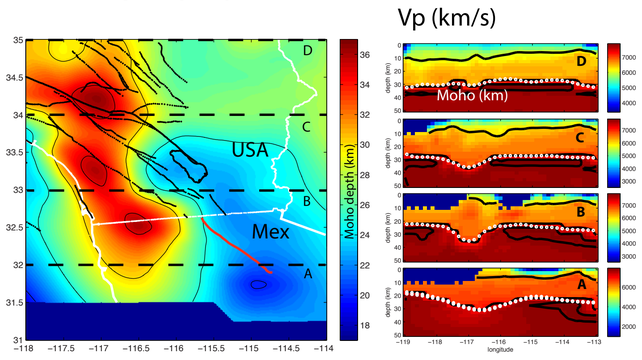

Vp (km/s)

(a) Moho depth indicates crustal thickness in the area, and in this area it shows thicker crust (~36 km) underneath the Pacific Peninsular and shallower crust (~20 km) below the Salton Trough. **(b)** East-west cross sections show Vp distribution from north to south. The white dashed lines indicate Moho depth that separates crust from upper mantle. There is a significant variation in crustal thickness from west to east. The EMC event (red line in **a**) occurred near the shallowest Moho.

Geodetic Measurements

GPS

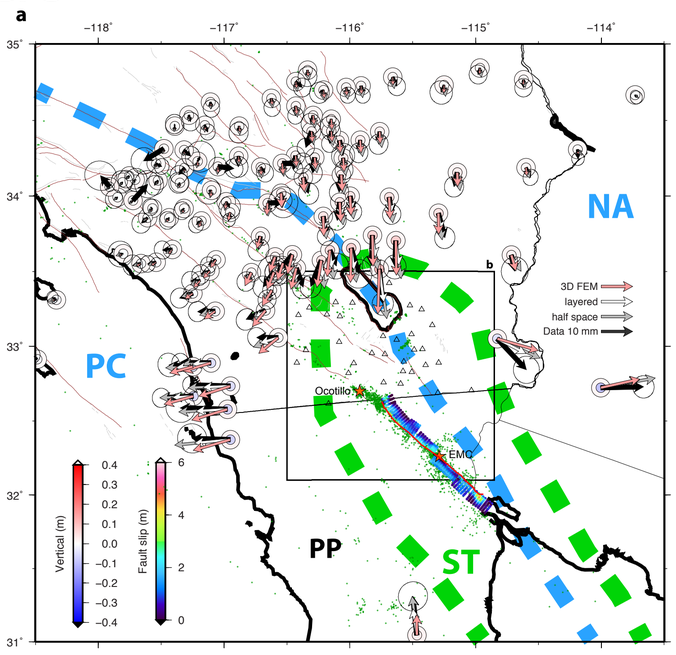

We obtain the EMC coseismic GPS measurements through the Plate Boundary Observatory (PBO) stations for the US side, and 3 additional campaign GPS measurements in Baja California, Mexico. The black arrows in **(a)** and **(b)** are horizontal displacements, and the white, grey, and pink arrows are model predictions with considering homogeneous, layered, and 3D elastic earth structures, respectively (see **Model Fitting** for detail). The greater colored circlesare GPS vertical displacement, and the smaller colored circles are model prediction based on the layered structure. The red line is the EMC surface rupture, and the color coded circles around it are modeled fault slip based on the layered structure. The red stars show the EMC main shock and the largest Mw 5.6 aftershock, and the green dots are aftershocks. The colored dashed lines show the tectonic blocks in the study area, where NA - North America; ST - Salton Trough; PP - Pacific Peninsular; PC - Pacific Plate.

InSAR

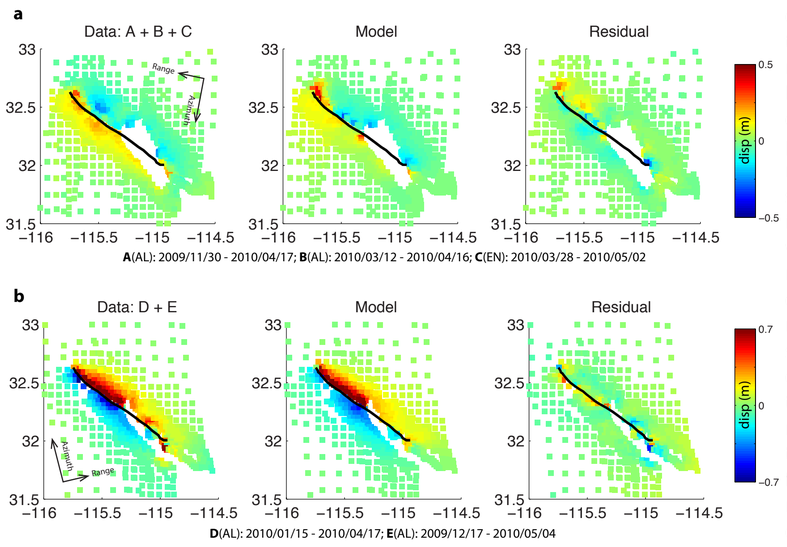

InSAR reveals surface displacement in line of sight (LOS) between the two acquisitions. In the figures, warm and cold colors represent range increase and decrease in LOS, respectively. **(a)** and **(b)** show InSAR coseismic displacement, predicted displacement (see **Model Fitting** below), and model residual for ascending and descending orbits, respectively. For descending orbit **(a)**, range increase represents westward motion and/or subsidence. The modeled coseismic displacement is based on the layered earth structure. The model residual shows higher residual near the surface rupture (black curved line), especially at the northern and southern tips of the rupture. This could be due to postseismic displacement that is included during the InSAR observation periods. Similarly, for ascending orbit **(b)** range increase represents eastward motion and/or subsidence, higher model residual also locates near the surface rupture.

Sub-pixel offset

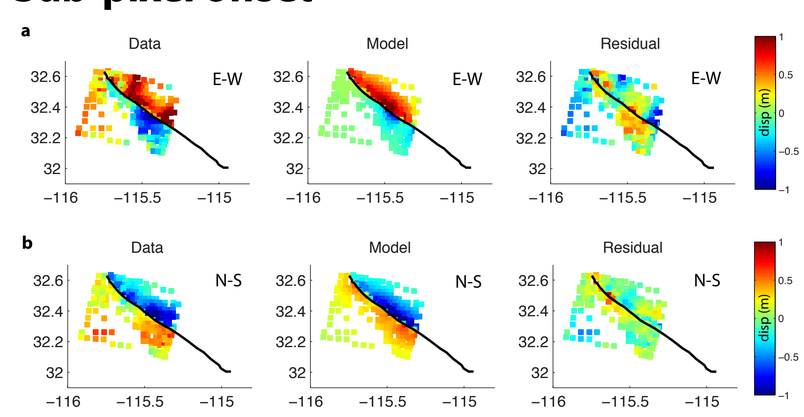

Sub-pixel offset calculates the cross-correlation between two acquisitions and converts to sub-pixel scale shift parallel and perpendicular to the satellite trajectory. Here we use SPOT satellite images that cover the northern portion of the fault surface rupture. We rotate the observed displacement into east-west **(a)** and north-south **(b)** directions. Sub-pixel offset method is generally noisier than InSAR because it directly compares correlation between pixels and is limited by the spatial resolution of pixels. The model residual shows higher misfit in the east-west direction at both near- and far fields.

Model Fitting

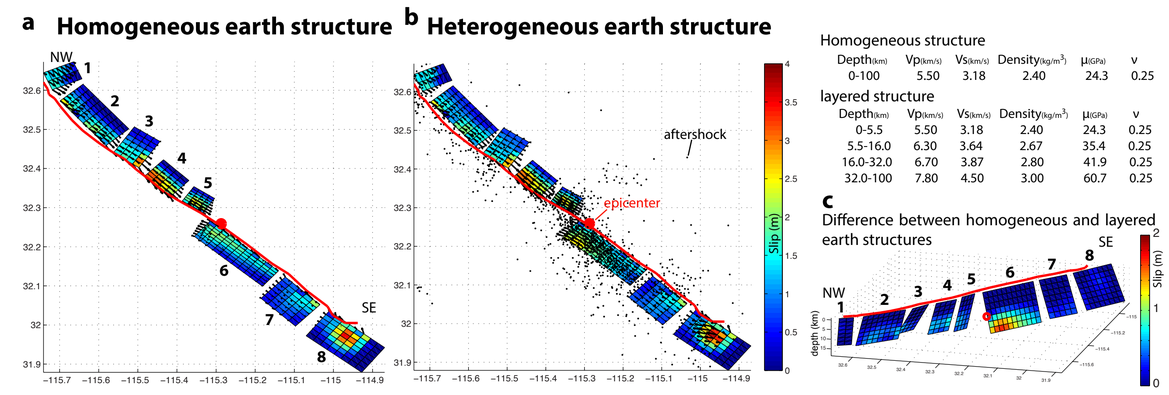

The 8-fault patch geometry and the strike/dip of each fault patch is optimized from surface rupture observations, aftershock relocations, and geodetic data. We divide each fault segment by several 2 × 2 km² subfaults, and each subfault has its own slip and rake. The amount of coseismic slip and rake of each sub-fault are inverted by least square fitting geodetic data including GPS, InSAR, and sub-pixel offset data in a homogeneous or a layered earth structure. The coseismic slip and rake distribution with considering **(a)** homogeneous and **(b)** layered earth structures are shown in figures above. Most of the slip occurs between 0 and 12 km in depth with predominately right-lateral strike-slip and minor normal motions. There is more slip located at segments 3, 4 ,and 8 in both earth structures. The difference (c) between homogeneous and layered structures mainly lies in the deeper part (below 10 km in depth) of the fault, which is due to higher shear modulus at the deeper part of the layered structure. The difference reaches ~1.6 m, which is 60% of slip in this region. This result implies a discrepancy in deep slip calculation due to choice of earth structures, and could result in incorrect result when estimating postseismic stress-driven afterslip and viscoelastic relaxation.

3D FEM layered model

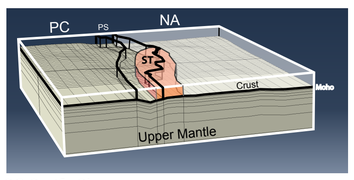

PC: Pacific Plate crust
PS: Pacific Peninsular crust
NA: North American Plate crust
ST: Salton Trough crust
The upper mantle is assumed homogeneous

We use 3D finite element model (FEM) to construct blocks for representing different tectonic regions. The model is composed of 5 different tectonic regions including Pacific Plate (PC), Pacific peninsular (PS), Salton Trough (ST), North American Plate (NA), and upper mantle. The boundary between crust and upper mantle is determined by Moho depth. The elastic moduli of each block are similar to the layered structure, but PC has relatively higher shear modulus due to the property of oceanic crust. We use the same slip distribution with layered earth structure as the coseismic slip input for the 3D model, and calculate the surface displacement for each GPS station. The pink arrows in the GPS map in the left show the model fitting to GPS stations. There is improvement in fitting due to thicker crustal thickness, which implies higher heterogeneity in the study.

Summary

- Complex fault-slip system during the EMC event
- Right-lateral strike-slip with normal dip-slip motion predominates coseismic slip
- Significant discrepancy in deep slip between different choice of earth structure
- Improvement in coseismic displacement model when consider 3D earth structure with lateral heterogeneity

National Aeronautics and Space Administration

Jet Propulsion Laboratory
California Institute of Technology
Pasadena, California

www.nasa.gov

Acknowledgements:

This work is in collaboration with H. Dickinson (Purdue Unv.), J. Sun (CEA, China), A. Freed (Purdue Univ.), and R. Burgmann (UC Berkeley). M.-H. Huang is supported by an appointment to the NASA Postdoctoral Program at the Jet Propulsion Laboratory, administered by Oak Ridge Associated Universities through a contract with NASA.

References:

Fletcher et al. (2014) Assembly of a large earthquake from a complex fault system: Surface rupture kinematics of the 4 April 2010 El mayor-Cucapah (Mexico) Mw 7.2 earthquake, Geosphere, 10, doi:10.1130/GES00933.1

Wei et al. (2011) Superficial simplicity of the 2010 El Mayor-Cucapah earthquake of Baja California in Mexico, Nat. Geo., 4, 615-618, doi:10.1038/NGEO1213

Poster No. EA-2

National Aeronautics and Space Administration

Earth System Model for Ice-Sheet/Solid-Earth/Sea-Level Coupling

Principal Investigator: Surendra Adhikari (329A-Affiliate)
Co-Is: Erik R. Ivins (329A) and Eric Larour (329D)

CONTEXT

- Modeling of ice sheets and their interactions with atmosphere, oceans, and solid-earth is essential for accurate predictions of sea-level (SL) change.
- Our research goal is to develop a system of models that can be constrained by geophysical, geodetic & astronomical data and investigate how Antarctic (AIS) & Greenland (GIS) ice sheets evolve in an ongoing warming climate.
- We present a new SL model as the first stepping stone toward this goal.

SEA-LEVEL MODEL: A NOVEL COMPUTATIONAL APPROACH①

Existing SL models operate on spectral domains, and are incompatible with finite-element ice-sheet models. We develop a mesh-based model (Fig. 1) that

- resolves (km-scale) high spatial resolution very efficiently, and
- parameterizes Green's functions more accurately!

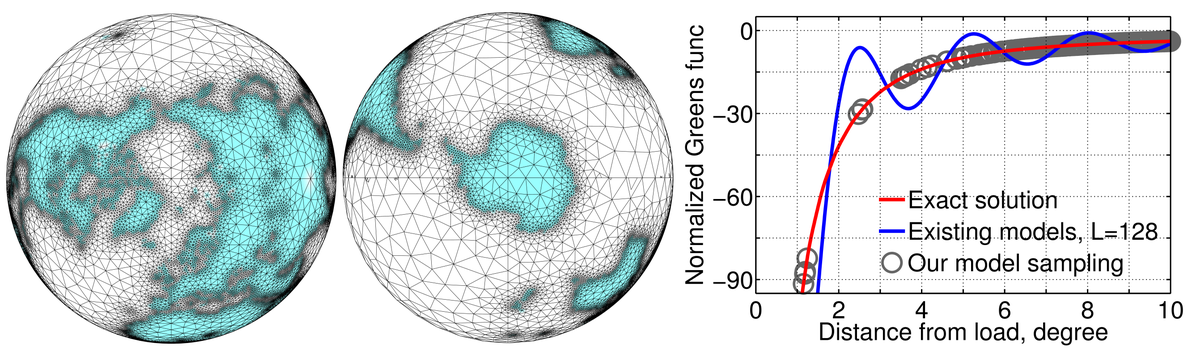

Fig. 1: A computationally efficient, numerically accurate, high-res SL model.

RESULTS: GEOPHYSICAL SIGNATURES OF ICE SHEETS

As example computations (Figs. 2-4), we force our model by monthly GRACE-based mass balance data of ice sheets for the period 2002 April - 2015 March.

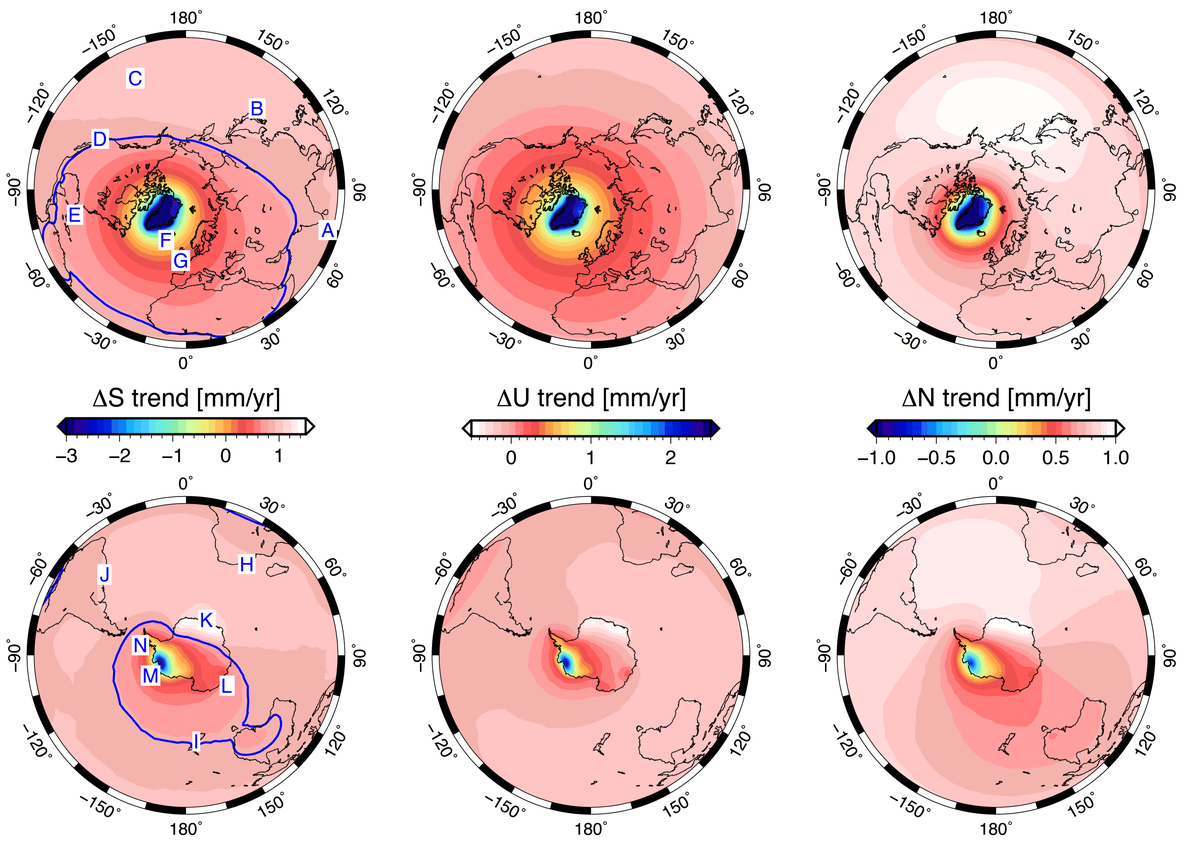

Fig. 2: Linear trends in SL change, ΔS, solid-earth deformation, ΔU, and geoid height, ΔN. Contours follow the global mean value (0.816 mm/yr).

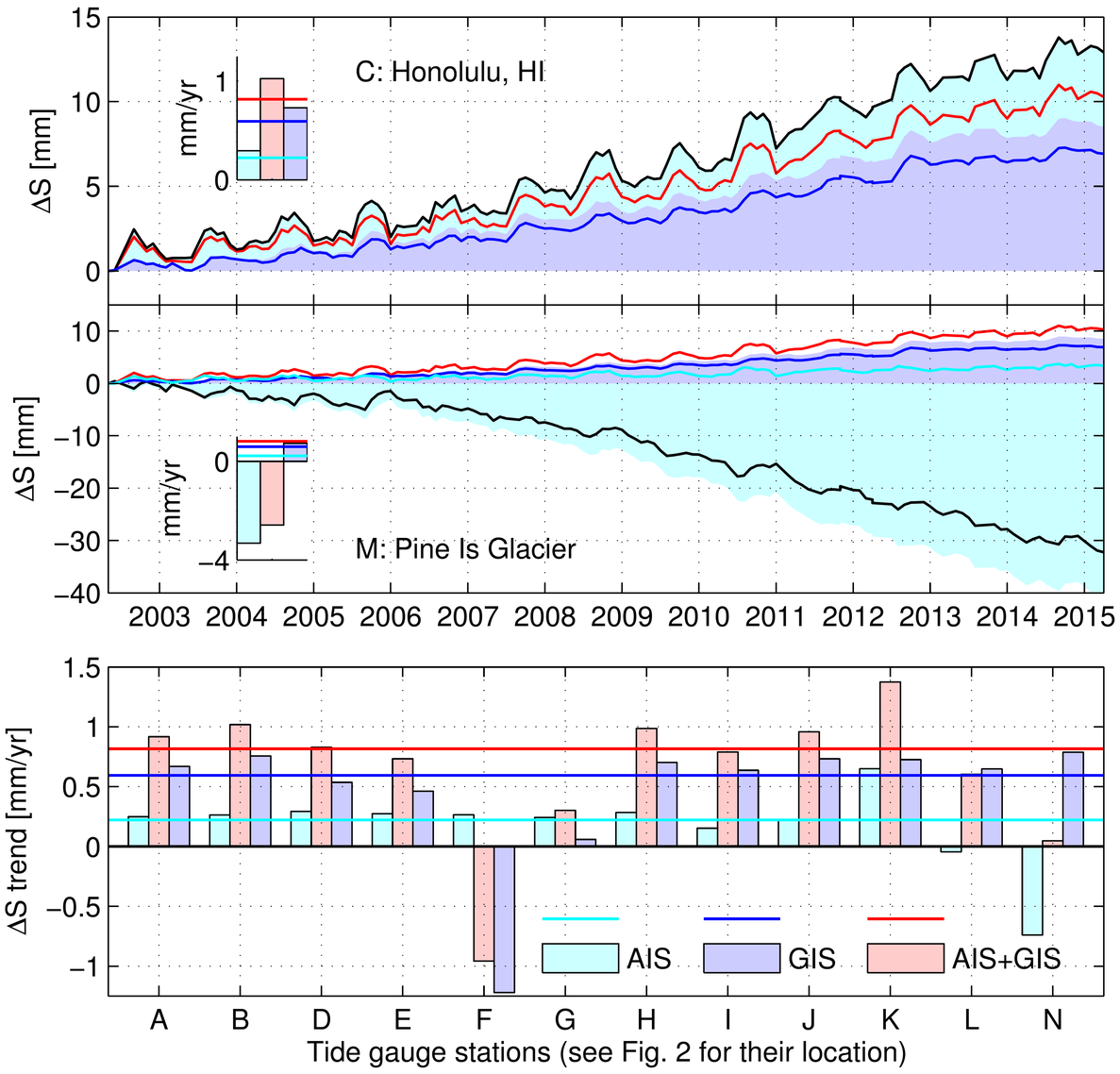

Fig. 3: Magnitudes and linear trends of SL change caused by individual ice sheets. Black lines are local ΔS; others represent global mean values.

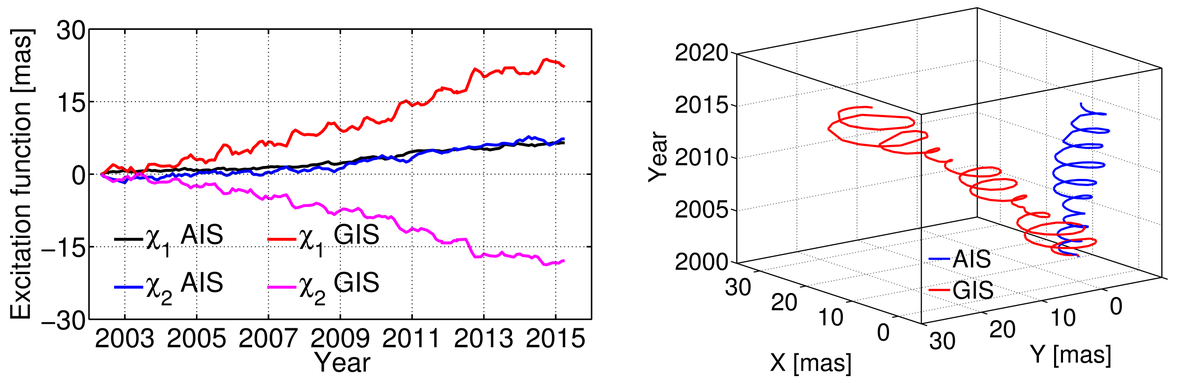

Fig. 4: Polar motion during the GRACE period: mass excitation functions (top left); monthly pole positions in the left-handed coordinates (top right); and ice sheets induced polar drift (right). Observed long-term (green arrow; Mitrovica et al., 2006) and recent (2005-2011; blue arrow; Chen et al., 2013) drift directions are also shown. [1 mas ≈ 3 cm]

SUMMARY

- We aim to improve SL predictions through accurate modeling of ice sheets by leveraging data-assimilation capability and computational architecture of JPL's Ice Sheet System Model (ISSM) and associated geophysical models.
- Toward this goal, we have developed a new mesh-based SL model that is easily integrable with ice-sheet models and has the following key feature:
  - It captures km-scale features in a few minutes (OS X 10.9.5); existing models require many hours to even resolve for, say, 50 km resolution.

①Adhikari, S., Ivins, E. R. and Larour, E., 2015, *Geosci. Model Dev. Discuss.*

National Aeronautics and Space Administration
Jet Propulsion Laboratory
California Institute of Technology
Pasadena, California

www.nasa.gov

This research was carried out at the **Jet Propulsion Laboratory** and the **California Institute of Technology** under a contract with the **National Aeronautics and Space Administration** and funded through the **NASA Postdoctoral Program** fellowship.

Poster No. EA-3

National Aeronautics and Space Administration

A Unified Land Surface Temperature and Emissivity Earth System Data Record (ESDR)

Nabin Malakar, Glynn Hulley, Pierre Guillevic, Simon Hook (329B)

Motivations

- NASA has identified a major need to develop long-term, consistent products with well-defined uncertainty statistics, termed Earth System Data Records (ESDR).
- Currently no such product exists that is providing global Land Surface Temperature and Emissivity (LST&E) products.
- We present our efforts to fulfill the need for ESDR for Global LST&E acquired from MODIS remote sensing instruments aboard Aqua and Terra platforms.
- The standard MOD11 use a split window approach, we are working on generating a new NASA LSTE product “MOD21” by using physics-based temperature emissivity separation (TES) algorithm. Validation of these products indicate that these products are complementary over graybody and barren sites. We exploit the unique advantages of each product to generate a unified LST product which has lower final uncertainties.
- Accurate knowledge of the LST&E at high spatial and temporal scales is a key requirement for many energy balance models to estimate important surface biophysical variables such as evapotranspiration and plant-available soil moisture. LST&E data are also essential for balancing the Earth's surface radiation budget.

MOD21: A New NASA LSTE Product

- We are working on generating a new NASA LSTE product at JPL (MOD21), which will be released as one of the collection 6 product in the near future.
- Validation Studies show that the new LSTE products are better retrieved on barren sites compared to the MOD11 LST product.
- Since the MOD21 and MOD11 tend to have complimentary accuracy over the barren and vegetative sites it makes sense to combine their strengths to generate the LST-ESDR.

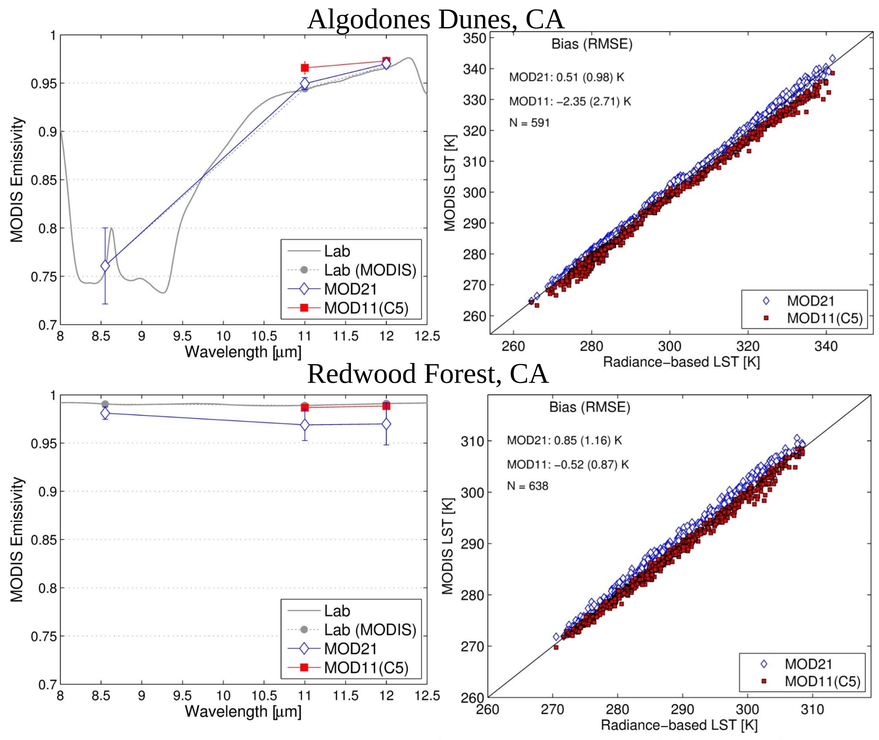

Figure 1. MOD21 emissivity and temperature validations for the Algodones Dunes, CA (top) and Redwood, CA (bottom) are compared with the emissivity lab references (left panels). Figures on the right show the temperature retrievals. The MOD21 product outperforms over the barren sites such as Algodones Dunes. MOD11 show consistent cold bias over the desert site. However, MOD11 products are better over the vegetation sites. The strengths of MOD21 and MOD11 are complementary in nature.

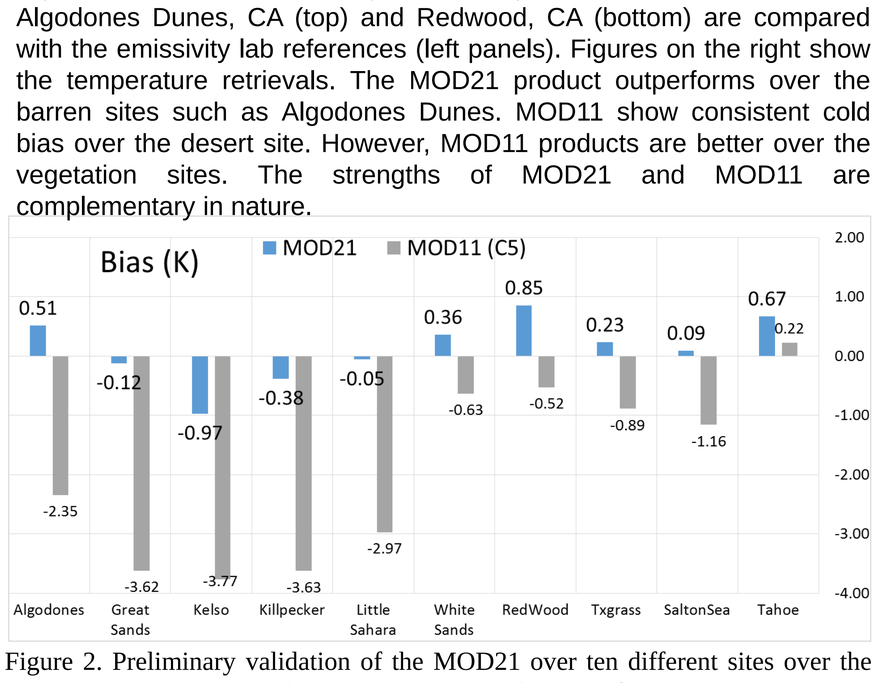

Figure 2. Preliminary validation of the MOD21 over ten different sites over the North America show that the MOD21 consistently outperforms in the barren sites as indicated by the Bias.

A Unified MODIS LST Product

- The MOD11 and MOD21 LST products can be merged using pre-defined uncertainties and a weighting rule based on a ‘ combination of states of information’ approach.
- The errors in LST are modeled as a function of view angle and the precipitable water content:

$$\delta LST_{MODIS} = a_o + a_1 PWV + a_2 \mathrm{SVA} + a_3 PWV \cdot SVA + a_4 PWV^2 + a_5 SVA^2$$

- The inverse of the LST errors are weighted and applied to the MOD11 and MOD21 LST products as follows:

$$\overline{LST} = \frac{1}{(w1 + w2)} (w1 \cdot LST_{MOD11} + w2 \cdot LST_{MOD21})$$

- The variances are combined to produce a final uncertainty estimate

$$\delta LST = (1/(w1 + w2))^{1/2}$$

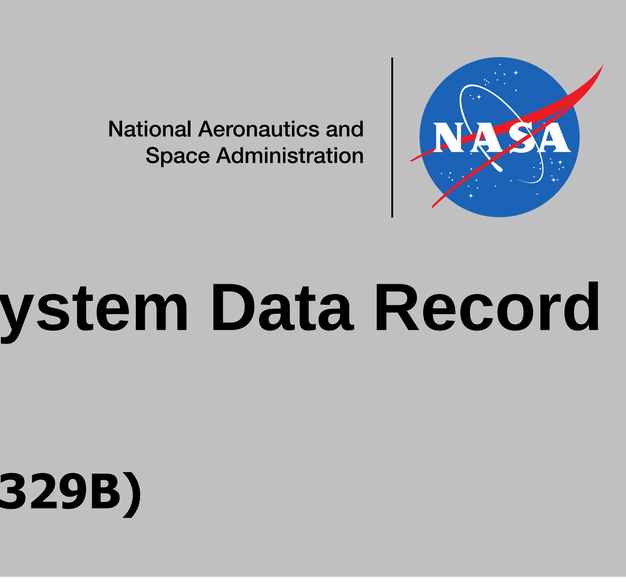

Figure 3. MODIS MOD07 precipitable water vapor (PWV) estimate (cm).

MOD21 LST | MOD11 LST | Unified MOD11+21 LST

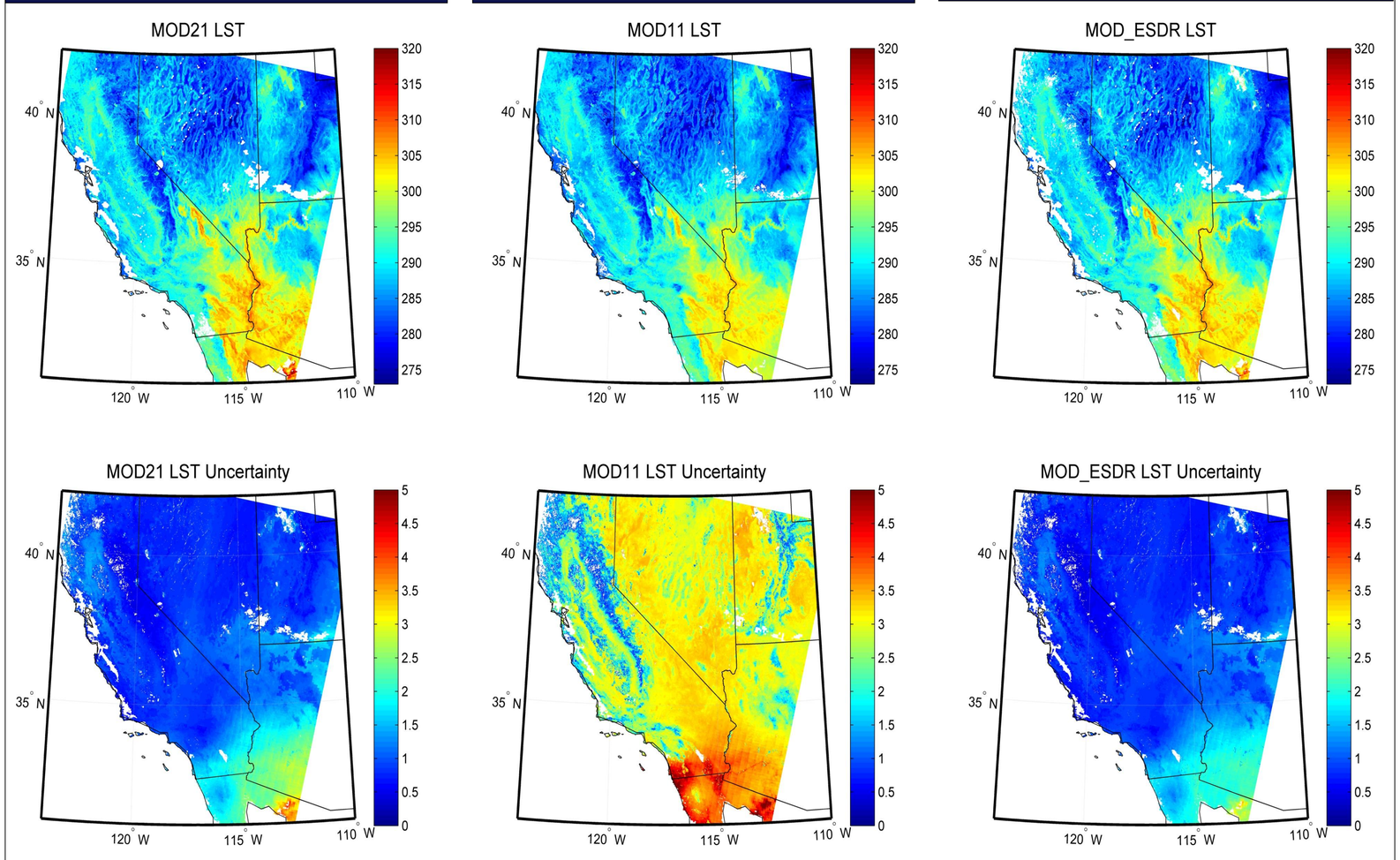

Figure 4. MOD21 (left) and MOD11 (middle) LST retrievals and associated uncertainties over the southwestern USA. The unified MOD11+21 LST product (right) is derived by using a combination of states of information approach.

MOD21 uncertainties are highest over humid regions over the Salton Sea and Imperial Valley agricultural district (southwest corner) shown in the MOD07 product (Figure 3), while MOD11 uncertainties are highest over bare regions of the Mojave desert and Colorado plateau (northeast corner). Note how the final uncertainties are lower than either of the original inputs since a ‘conjunction’ of probabilities of each product’s uncertainty is calculated.

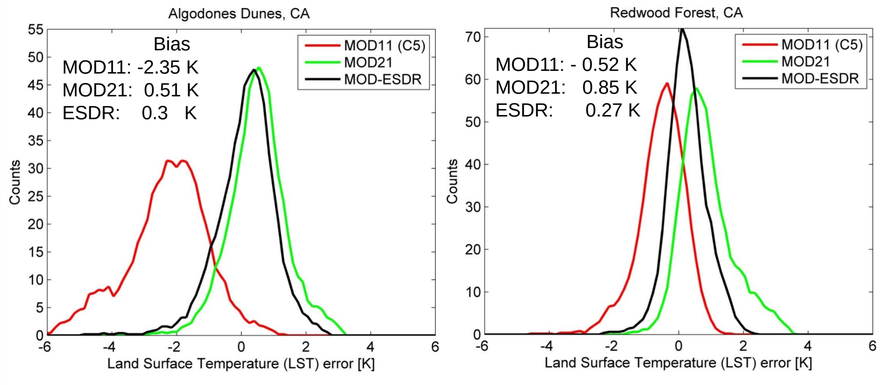

Figure 5 The unified product (solid black line) utilizes the strength of both MOD21 and MOD11 products. As seen, it is closer to the MOD21 in barren site (left) and remains in between the two for graybody site (right).

Conclusions

- A new NASA LST&E product (MOD21) has been developed at JPL that shows consistent accuracy across all land cover types (1-1.5 K) and produced a physically retrieved emissivity for MODIS bands 29, 31 and 32.
- As part of a NASA MEaSUREs project, a unified LST&E database is currently being produced by merging the heritage MOD11 and new MOD21 LST products to produce a long term data record with well defined uncertainties.
- Validation studies have shown the unified product to have higher LST accuracy than either of the two products used to produce it (MOD11/21).

National Aeronautics and Space Administration

Jet Propulsion Laboratory
California Institute of Technology
Pasadena, California
www.nasa.gov

Poster No. EA-4

National Aeronautics and Space Administration

A physics-based algorithm for simultaneous retrieval of land surface temperature and emissivity from VIIRS thermal infrared data

Tanvir Islam*, Glynn C. Hulley, Nabin Malakar, Pierre C. Guillevic, Simon J. Hook
***tanvir.islam@jpl.nasa.gov**

INTRODUCTION

This study presents a physics based algorithm for simultaneous retrieval of land surface temperature (LST) and emissivity fields in the thermal infrared bands from the recently launched Suomi National Polar-orbiting Partnership's (NPP) Visible Infrared Imaging Radiometer Suite (VIIRS) payload. The algorithm, known as temperature emissivity separation (TES) algorithm, is developed by removing the atmospheric effects from the at-sensor radiances using a fast radiative transfer model - Radiative Transfer for (A)TOVS (RTTOV), thus isolating the surface radiance contributions.

VIIRS TES ALGORITHM

NASA VIIRS LST and Emissivity Product

NASA LST&E Products	Status	Spatial	Formats	Atmospheric Correction	Algorithm	Science Data Products
VIIRS-TES	Under development at JPL (Algorithm delivery Jan 2016)	750 m	L2 Swath, L2G L3 Grid, 1:30 am/pm	MERRA/NCEP/ECMWF + Water Vapor Scaling (WVS) model	Temperature Emissivity Separation (TES)	- LST - Emissivity (bands 14, 15, 16)

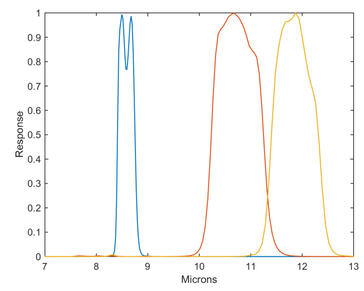

Spectral response functions for the three VIIRS thermal infrared bands (M14, M15, and M16).

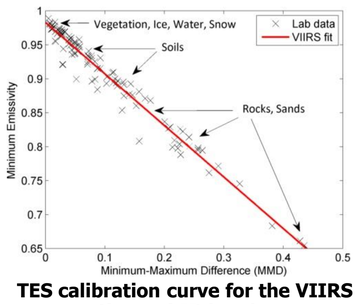

TES calibration curve for the VIIRS thermal IR bands.

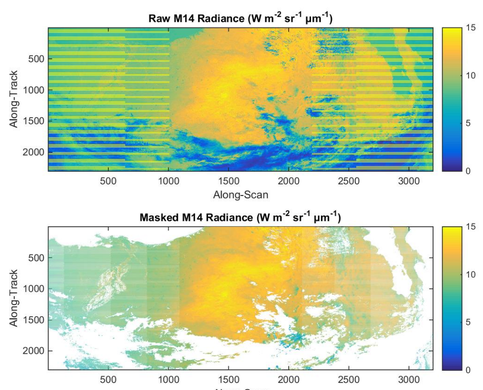

A masking example illustrating the screening of unwanted pixels in the M14 satellite VIIRS radiances

- The TES calibration curve is determined by using a broad range of surface materials such as vegetation, ice, water, snow, soils, rocks, and sands.

ATMOSPHERIC CORRECTION IMPACT

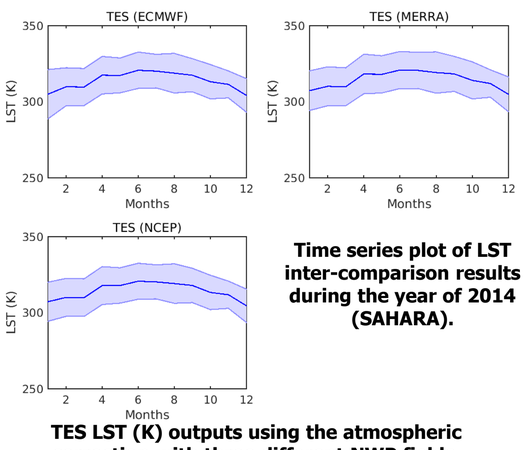

Time series plot of LST inter-comparison results during the year of 2014 (SAHARA).

TES LST (K) outputs using the atmospheric correction with three different NWP fields.

Region	NWP Type	Mean	STD
CONUS	ECMWF	272.54	27.96
	MERRA	273.02	28.09
	NCEP	272.98	28.13
SAHARA	ECMWF	351.28	39.10
	MERRA	352.13	39.10
	NCEP	351.30	38.40

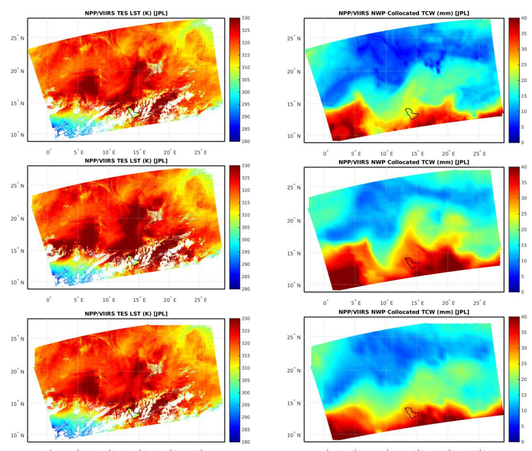

VIIRS TES LST outputs and the corresponding collocated NWP total column water vapor (TCW) fields on the VIIRS granule.

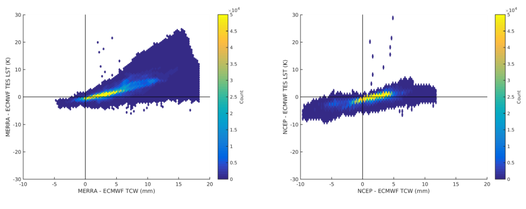

VIIRS TES LST outputs and the corresponding collocated NWP total column water vapor (TCW) fields on the VIIRS granule.

LST ASSESSMENT

Validation Site	NWP Type	MB	MAE	RMSE	r	STD
Tahoe	ECMWF	-0.14	0.75	1.06	0.99	1.10
	MERRA	-0.13	0.83	1.15	0.99	1.20
	NCEP	-0.23	0.79	1.13	0.99	1.17
Salton Sea	ECMWF	-0.93	2.30	2.93	0.90	2.93
	MERRA	-0.72	2.18	2.74	0.91	2.79
	NCEP	-0.73	2.58	3.17	0.88	3.26

- VTES LST (K) assessment statistics against JPL radiometer measurements.
- Results suggest that the TES algorithm compares reasonably well to the independent validation datasets.
- No single NWP product is found to be superior to the others for atmospheric correction, and their performance varies on a "case by case" basis.
- Overall, based on bulk statistics, TES derived outputs from the different NWP driven atmospheric corrections agree very well, within 1 K, and apparently, any of the NWP products can be used within the TES system.

EMISSIVITY ASSESSMENT

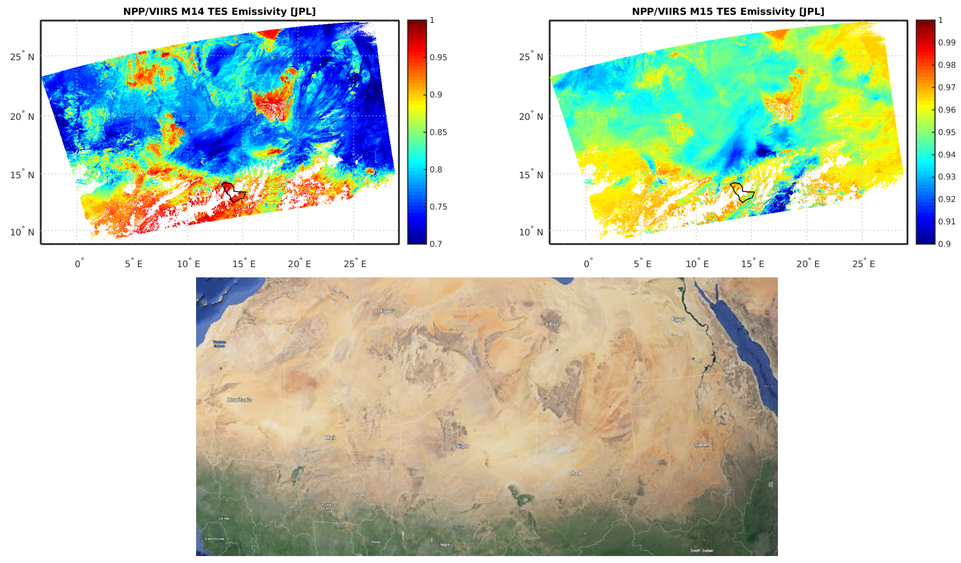

NPP/VIIRS emissivity at band M14 (top left) and M15 (top right) using the TES algorithm. ECMWF analysis thermodynamic profiles are used for the atmospheric correction. Corresponding visible imagery is also shownM14 satellite VIIRS radiances

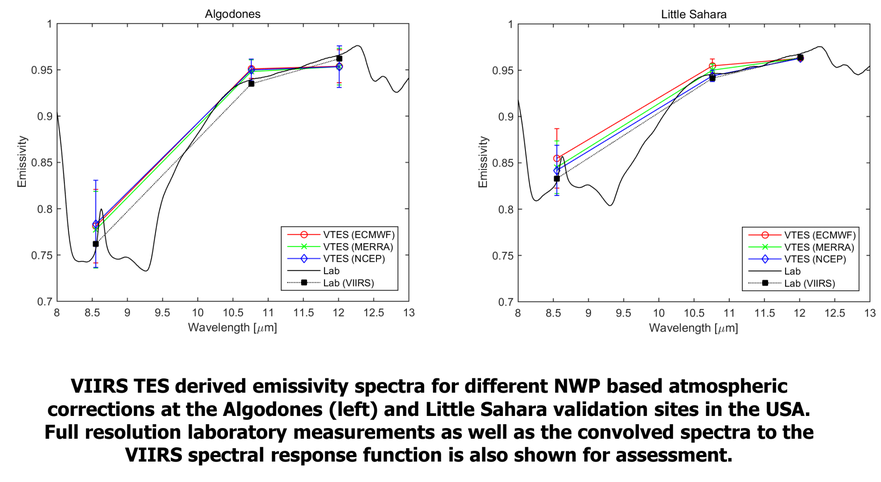

VIIRS TES derived emissivity spectra for different NWP based atmospheric corrections at the Algodones (left) and Little Sahara validation sites in the USA. Full resolution laboratory measurements as well as the convolved spectra to the VIIRS spectral response function is also shown for assessment.

FUTURE RESEARCH

- Implementing water vapor scaling method in the TES
- Improved emissivity dependent EMC/WVD algorithm
- MODIS/VIIRS continuity for Climate Data Record
- Radiance based validation

National Aeronautics and Space Administration

Jet Propulsion Laboratory
California Institute of Technology
Pasadena, California

www.nasa.gov

Poster No. EA-5

National Aeronautics and Space Administration

Assessing ecosystem response to droughts using satellite passive microwave observations

Principal Investigator: Dimitrios Stampoulis (329C)
Konstantinos M. Andreadis (329C) and Stephanie L. Granger (329M)

I. Background and objectives

- Explore the relations between water dynamics and ecosystem processes by investigating the response of vegetation and soil moisture to precipitation anomalies, with a special focus on water-limited ecosystems.
- The most commonly used global observations of vegetation dynamics are based on the spectral vegetation indices, such as NDVI, but are plagued by several shortcomings.
- Passive microwave observations from space, however, are sensitive to water content at the surface, and thus consist a critical tool that can be used towards the investigation of how water dynamics and ecosystem processes interact, especially under extreme hydrologic conditions.

II. Study area and data

Study area: East Africa

3 major land-cover categories

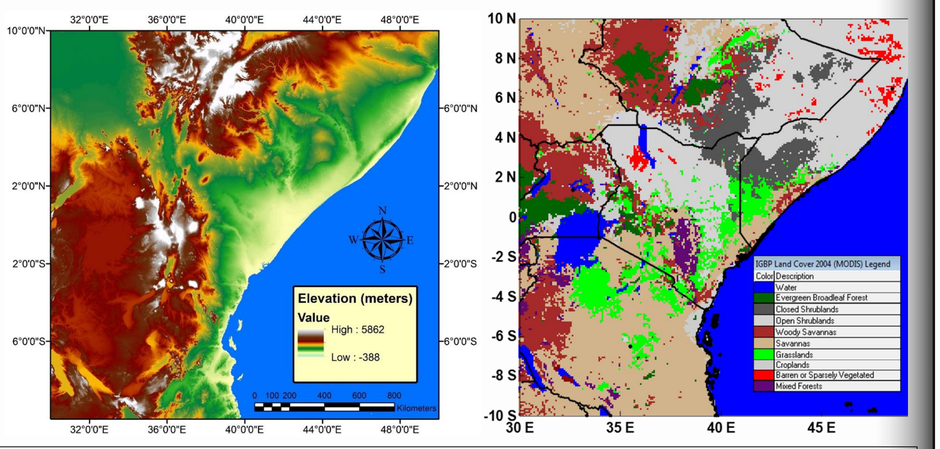

Precipitation: TRMM 3B42 V7 (daily)
Vegetation Water Content (VWC): NRL WindSat VWC algorithm (daily)
Soil Moisture (SM): NRL WindSat SM algorithm (daily)
Analysis: daily/TRMM nominal resolution for 2003-2011

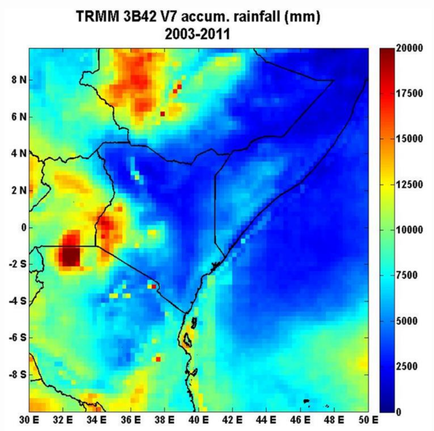

NDVI/EVI (8-day/0.05 deg) from MODIS TERRA & AQUA for comparison with WindSat VWC algorithm

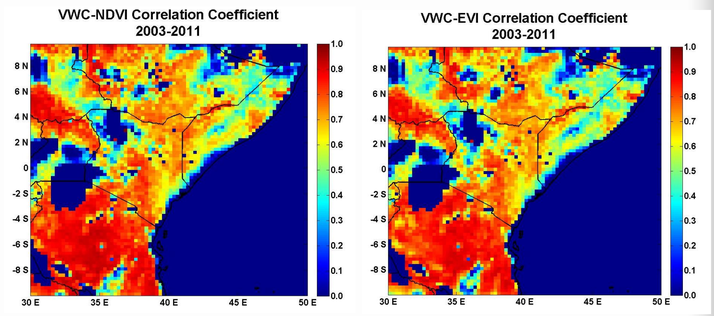

Space-average time series for the three major vegetation categories

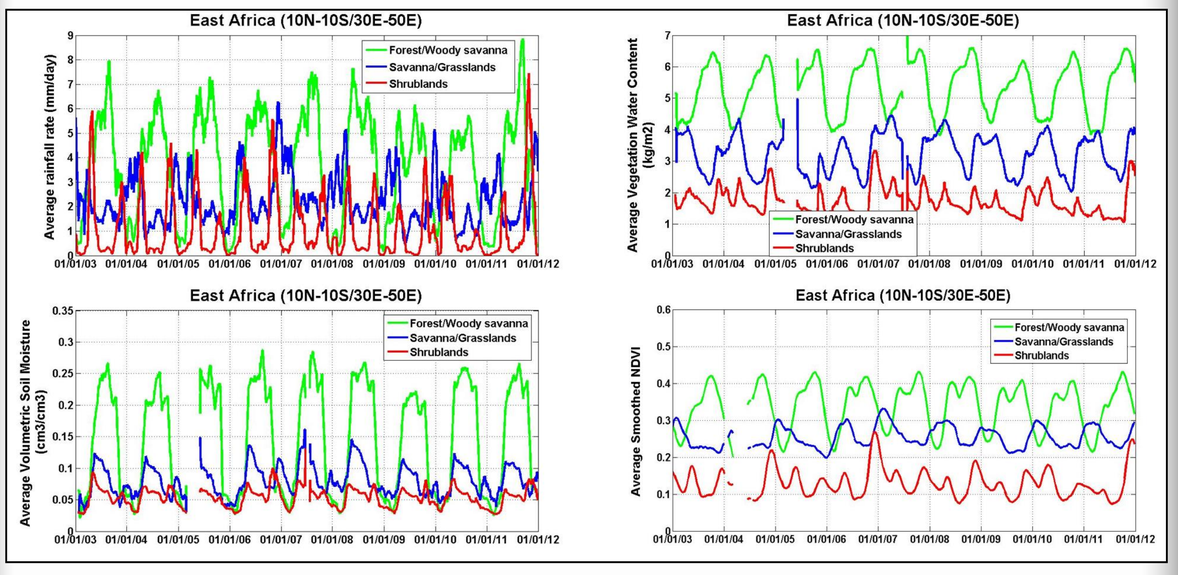

III. Identifying dry spells

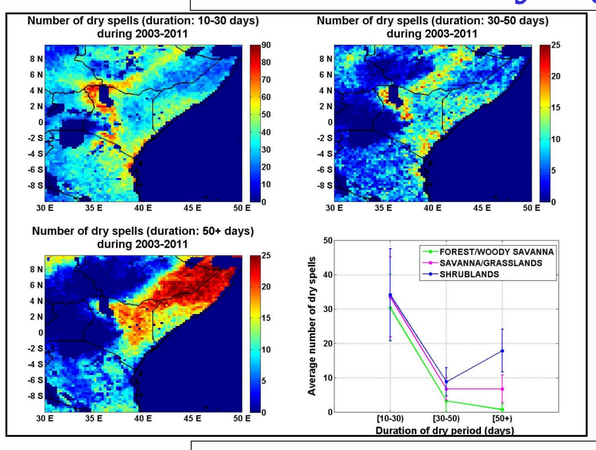

How does the number of dry spells change among the various vegetation regimes and for different duration thresholds?

The majority of short- and medium-duration dry spells occur in the central and eastern parts of East Africa, while the long-duration dry periods occur only over the semi-arid shrublands.

IV. VWC/SM response

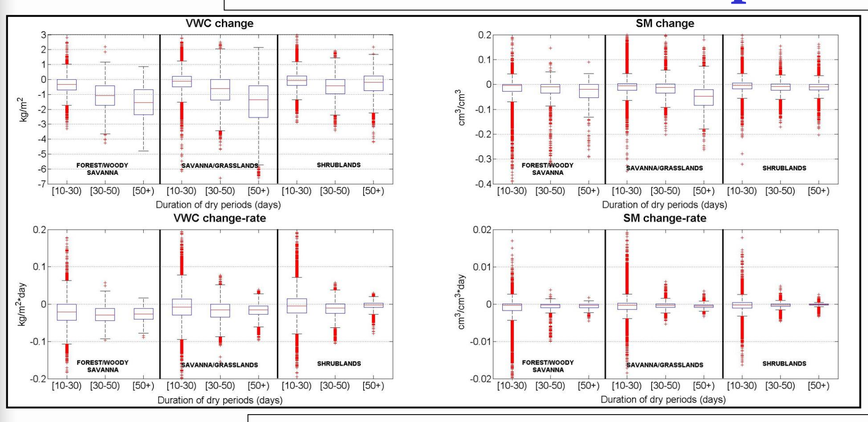

Boxplots of VWC/SM change and change-rate values for the 3 main land-cover categories in East Africa and for different dry-period duration thresholds.

V. VWC/SM resilience

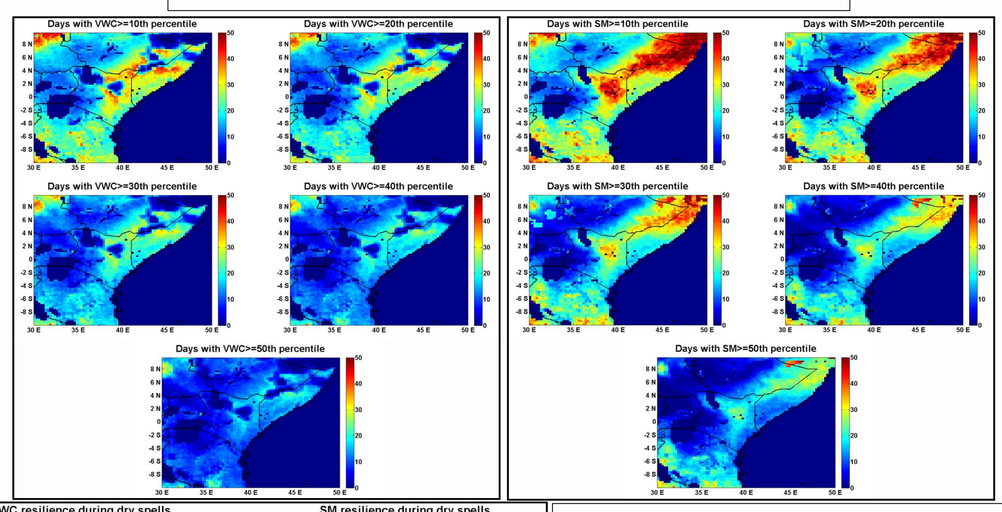

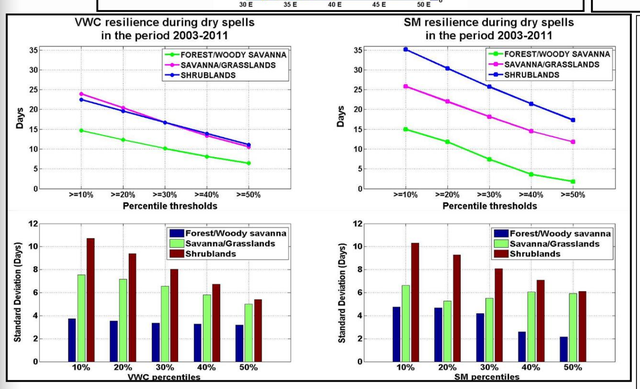

Resilience is the ability, measured in time, to maintain the normal state; it is characterized by the persistence of the system in maintaining its stability. Exceedance of various VWC and SM thresholds is investigated among the three main vegetation regimes.

VI. Conclusions

- Each of the three major land-cover categories in East Africa is characterized by a unique hydro-climatic profile.
- In general, the longer the dry spell, the greater the loss of VWC/SM is. However, the xerophytic shrubland-type vegetation exhibits more mesic conditions, and in many cases VWC increases during long dry spells.
- The drier parts of East Africa are characterized by higher VWC and SM resilience, whereas the wettest ones are more quickly affected by precipitation deficiencies.
- SM is more resilient than VWC over dry regions (east & south) and less resilient than VWC in the wet regions (west & north).

National Aeronautics and Space Administration

Jet Propulsion Laboratory
California Institute of Technology
Pasadena, California
www.nasa.gov

Poster No. EA-6

National Aeronautics and Space Administration

Learning from SMAP: Improving radar-only soil moisture retrieval

Principal Investigator: Mariko Burgin (329C)
Eni G. Njoku (3290), Jakob van Zyl (1000)

Objectives
- Intercomparing SMAP with other global soil moisture products to determine the differences and improvements brought by SMAP
- Explore the possibility of an improved radar-only algorithm, tested on Aquarius data

Soil Moisture Active Passive (SMAP) mission
- Launched January 31, 2015
- Collects global radiometer (36 km) and radar (3 km) measurements at L-band every 3 days
- Provides soil moisture content of the upper ~5 cm of soil based on passive (L2 SM P at 36 km), active-passive (L2 SM AP at 9 km), and active (L2 SM A at 3 km) retrieval methods

The opportunity
Leverage high-resolution radar (HH, VV, HV) data to obtain a high-resolution soil moisture product

\+ Higher resolution
+/– Sensitive to surface roughness and vegetation geometry
– Complex forward models

Current radar algorithms
- Depend on ancillary data
  - ➔ Land cover: MODIS International Geosphere-Biosphere Programme (IGBP) classification
  - ➔ Vegetation: Normalized Difference Vegetation Index (NDVI), Vegetation Water Content (VWC)
- Make assumptions or ignore specific modeling aspects
  - ➔ Soil surface roughness
  - ➔ Vegetation seasonality, terrain topography

How does SMAP compare to other soil moisture products?
- Re-grid to EASEv2 36 km
- Apply product-specific flagging

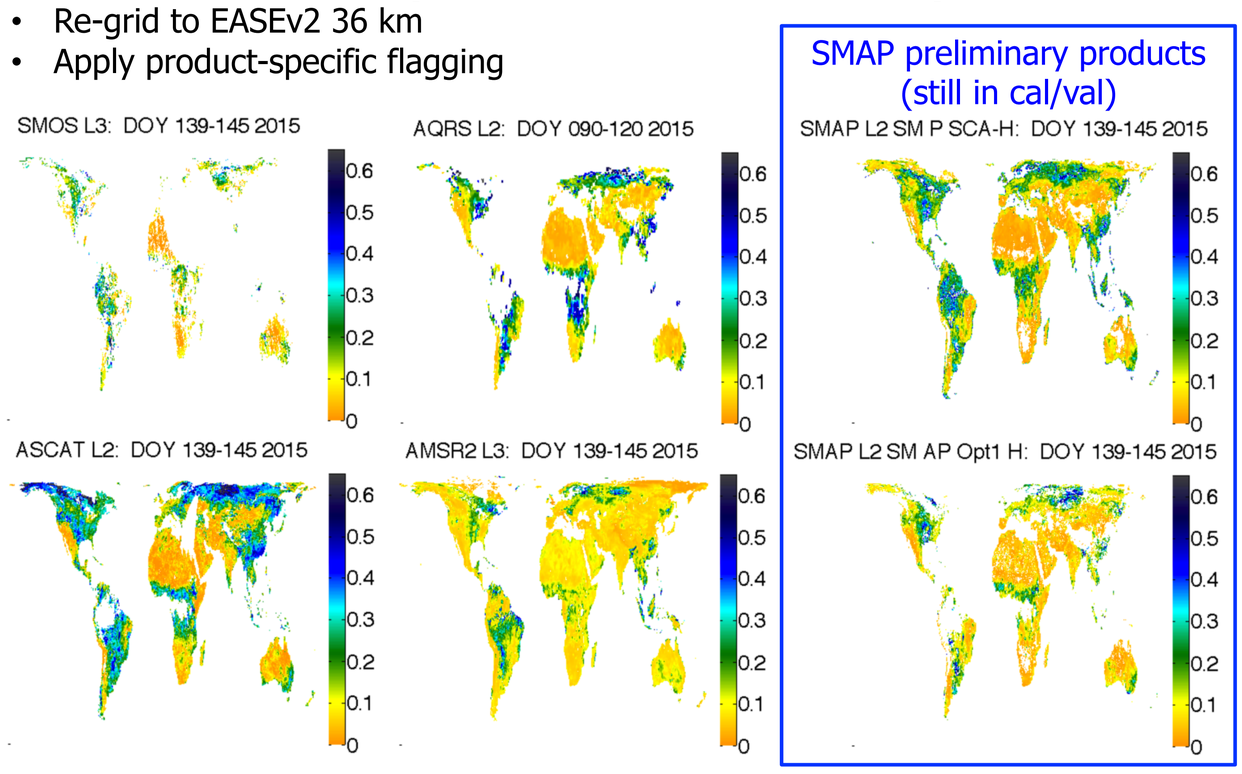

Soil moisture products differ significantly
- ESA SMOS (L-band) requires strict flagging for RFI and dense vegetation
- NASA Aquarius (L-band) shows wetter trends in wet soil moisture range
- EUMETSAT ASCAT (C-band) is wetter in medium to wet soil moisture ranges and in Northern latitudes. ASCAT soil moisture index is converted to volumetric soil moisture via soil porosity
- JAXA GCOM-W AMSR2 (C-band) shows compressed soil moisture range and overall dry bias

➔ Intercomparison helps to improve SMAP algorithms
➔ Besides SMAP, only ASCAT delivers a global radar-only soil moisture product

Studying an empirical soil moisture algorithm with Aquarius data
Using 2.5 years of L-band Aquarius data to derive weekly parameter (*a*, *b*) at EASEv2 36 km
- Aquarius L3 gridded 1-deg weekly soil moisture (v2) retrieved from radiometer data
- Aquarius radar data corrected to 40° incidence angle, average of de/a-scending overpasses
- Utilizing MODIS IGBP land cover classification map

➔ Investigate seasonal changes with a 3-month moving window

Empirical relationship between radar backscatter (σ_{HH}, σ_{VV}, σ_{HV} in dB) and soil moisture (sm in cm^3/cm^3)

$$\sigma_{HH} = a_{HH}*sm + b_{HH}$$
$$\sigma_{VV} = a_{VV}*sm + b_{VV}$$
$$\sigma_{HV} = a_{HV}*sm + b_{HV}$$

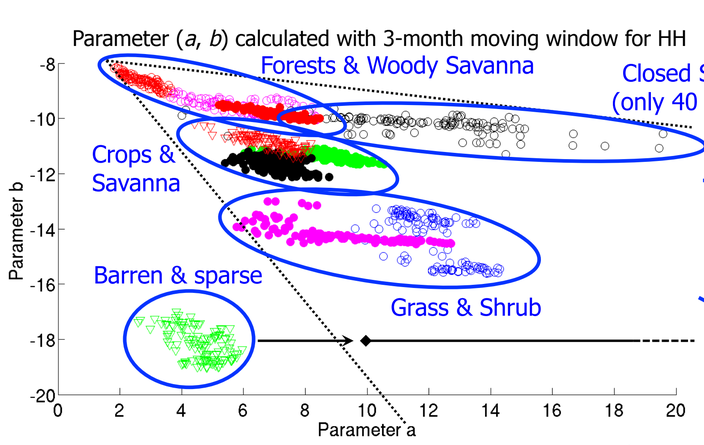

Parameter (*a*, *b*) based on a 3-month moving window for HH. Each point represents the global average over an IGBP class for a specific week
- ➔ Spread out neatly in *b* ranging from sparse to dense vegetation
- ➔ Soil moisture variability captured in *a*
- ➔ Parameter (*a*, *b*) show seasonality
- ➔ Barren & sparse land cover class becomes noise limited over Saharan desert, Saudi Arabian Peninsula and Mongolian Highlands

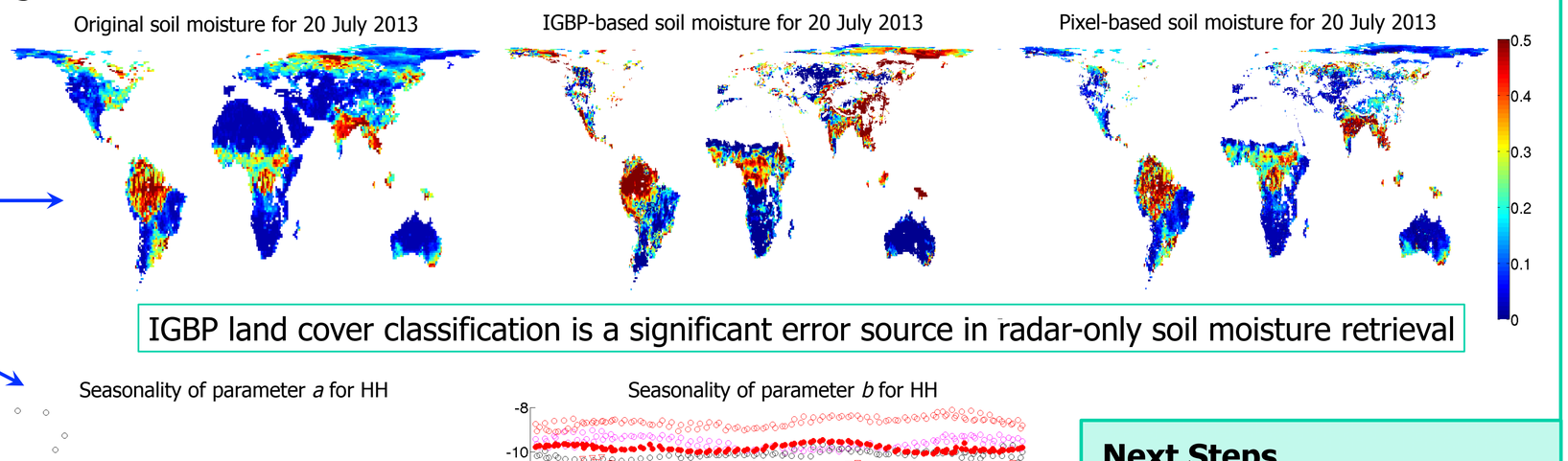

IGBP land cover classification is a significant error source in radar-only soil moisture retrieval

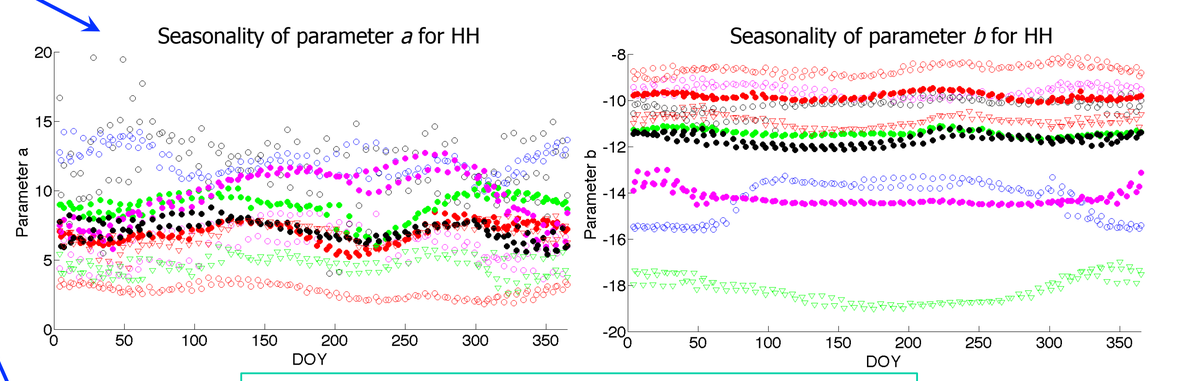

Vegetation seasonality can be significant

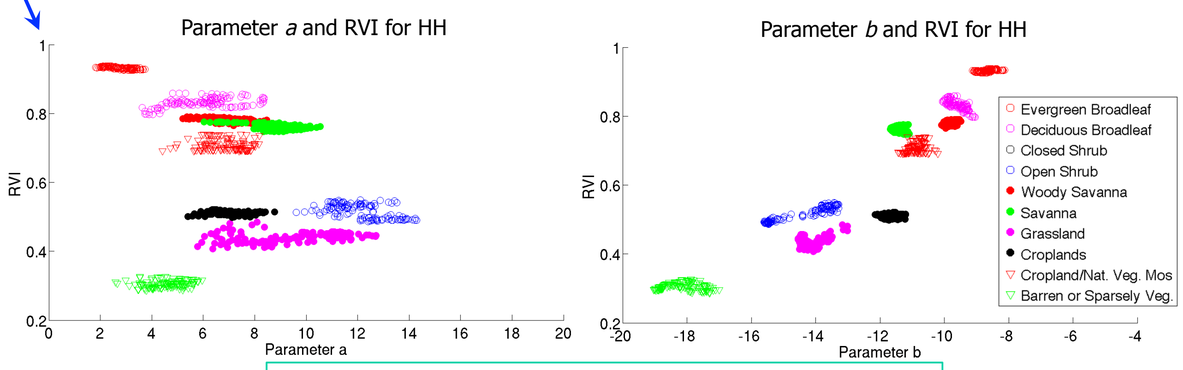

RVI can be used as vegetation indicator

$$RVI = \frac{8\,\sigma_{HV}}{\sigma_{HH} + \sigma_{VV} + 2\,\sigma_{HV}}$$

Radar vegetation index (RVI)

Next Steps
- Update parameter (*a*, *b*) based on SMAP 3 km radar and 36 km radiometer-derived soil moisture
- Utilize radar data to globally classify land cover types
- Include vegetation seasonality in estimation algorithm via RVI
- Derive parameter (*a*, *b*) using modeled data such as from NASA Goddard Earth Observing Assimilation (GMAO) and European Center for Medium-Range Weather Forecasts (ECMWF)

Poster No. EA-7

National Aeronautics and Space Administration
Jet Propulsion Laboratory
California Institute of Technology
Pasadena, California

www.nasa.gov

National Aeronautics and Space Administration

Near-real time monitoring of the Californian drought with the Airborne Snow Observatory

Principal Investigator: K.J. Bormann[1]

T.H. Painter[1], D. Marks[2], B. McGurk[3], A. Hedrick[2], A. Winstral[4], J.S. Deems[5]

Background

- CA is undergoing a large multi-year hydrological drought, largely caused by precipitation deficiencies.
- Hydrological drought is best characterized using streamflow observations and water reserve levels but meteorological droughts caused by precipitation deficiencies are often characterized using spatially distributed precipitation estimates (e.g. droughtmonitor.unl.edu – Figure 1)

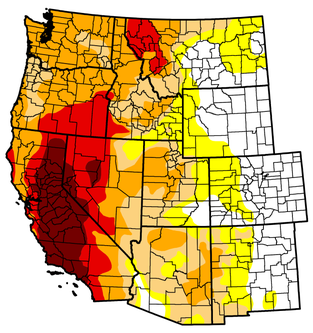

Figure 1 – U.S. Drought Monitor 7/7/2015

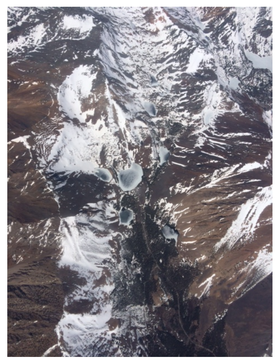

Figure 2 – The view from the ASO plane

- Spatially distributing precipitation in complex terrain is challenging due to orographic effects and local terrain features. Furthermore, estimating the phase of precipitation (snow/rain) adds further complexity in snow-prone areas.
- Due to sparse rain gauge networks, that are often missing at the very high elevations, and inefficiencies in collections we have a limited grasp of actual precipitation patterns.
- Until recently, in order to monitor drought conditions in the mountains in near-real time, we had to rely on statistical or physically-based models that come with largely unknown uncertainty.

Airborne Snow Observatory & Data

- ASO is equipped with the latest technology and is capable of directly observing snow deposition patterns using retrievals from both before and after a snow storm.
- ASO has been operating since 2013 and directly measures the snowpack at high spatial (3m) and temporal scales (weekly), with a 24 hour data turnaround.
- ASO takes advantage of recent technology advances in LiDAR instrumentation (Figure 3) to produce an unprecedented data stream.
- From these data we can conduct observations-based mass balance accounting of precipitation (using snowfall in the mountains), and evaluate our understanding and methods for distributing high altitude precipitation.

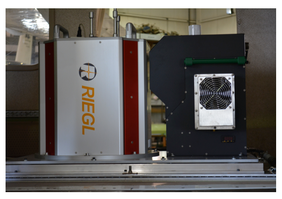

Figure 3 – Riegl LMS-Q1560 Lidar & CASI 1500 spectrometer

- The new data provide a vast improvement in the combined spatial and temporal scales than we can achieve with alternative remote sensing methods and the traditional snowcourse measurements.
- The ASO compliments other water resource initiatives at JPL, such as GRACE, SMAP, SWOT, by providing a basin-scale operation that is more nimble than satellite-based efforts and able to operate at spatial and timescales that are important for water management.

Research Question

How will improved knowledge of the spatial distribution and overall quantity of snow water resources from ASO change our current understanding of water balance components in snow-prone mountainous basins?

Approach

- Tuolumne Basin, CA – study region (Figure 4)
- Compare water balance components between iSnobal (the snow model) along with the ASO observations (Figure 5), with observed runoff (considered to be the best indicator of the "truth")

Figure 4 – Location of study region

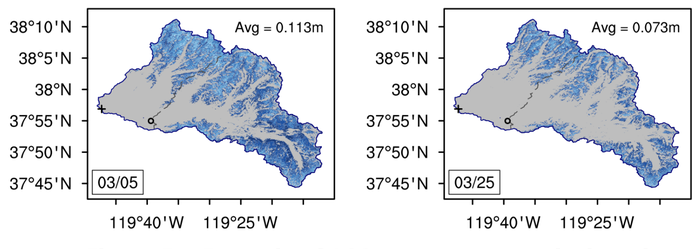

Figure 5 – Example of ASO snow water equivalent data for two 2015 surveys in the Tuolumne.

National Aeronautics and Space Administration

Jet Propulsion Laboratory
California Institute of Technology
Pasadena, California

www.nasa.gov

Affiliations:-
1 Jet Propulsion Laboratory, California Institute of Technology, Pasadena, CA, USA
2 United States Department of Agriculture, Agricultural Research Service, Northwest Watershed Research Center, Boise, ID, USA

Results

- Streamflow inflows to the Hetch Hetchy reservoir (San Francisco's water supply storage) show the severity of the current drought (Figure 5)
- Annual water volumes also reflect this drought signal in the long-term context (Figure 6)

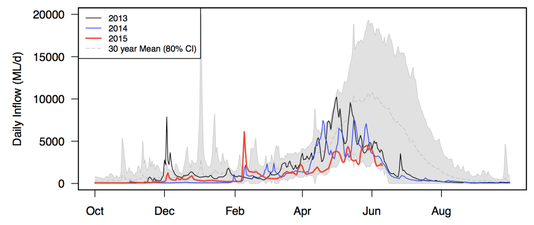

Figure 5 – Daily reservoir inflows for the period of ASO operation

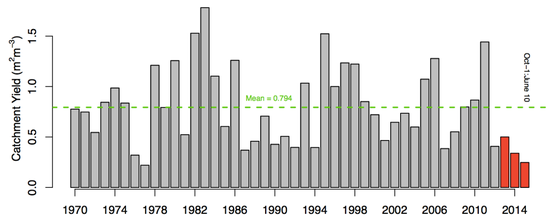

Figure 6 – Annual reservoir inflows since 1970

- ASO only captures the snowfall (and cannot detect liquid precipitation) but we do have the capability to observe precipitation patterns.
- The presumed lapse rates that predict increasing precipitation rates with altitude are not observed (Figure 7).

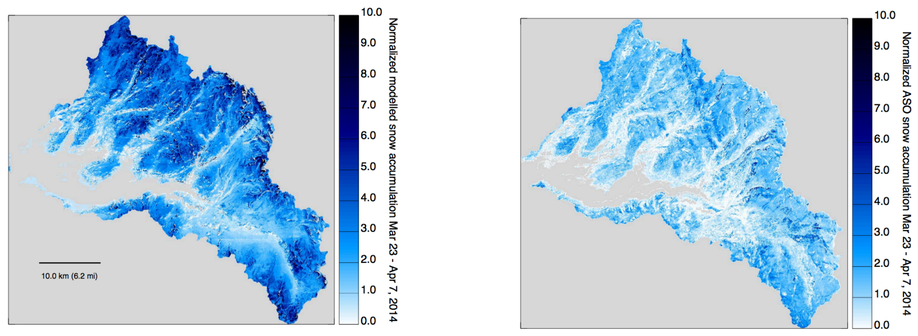

Figure 7 – Normalized weekly snow deposition for modelled precipitation (left) and ASO observed snowfall (right) for a significant storm event April 28, 20114.

ASO estimates that snowmelt contributes a mean of 80% to streamflows during the drought. The model estimates are much higher.

More precipitation fell as rainfall in late spring 2015 than in other years. Which helps to explain much increased basin ET losses and subsequent forecasting difficulties.

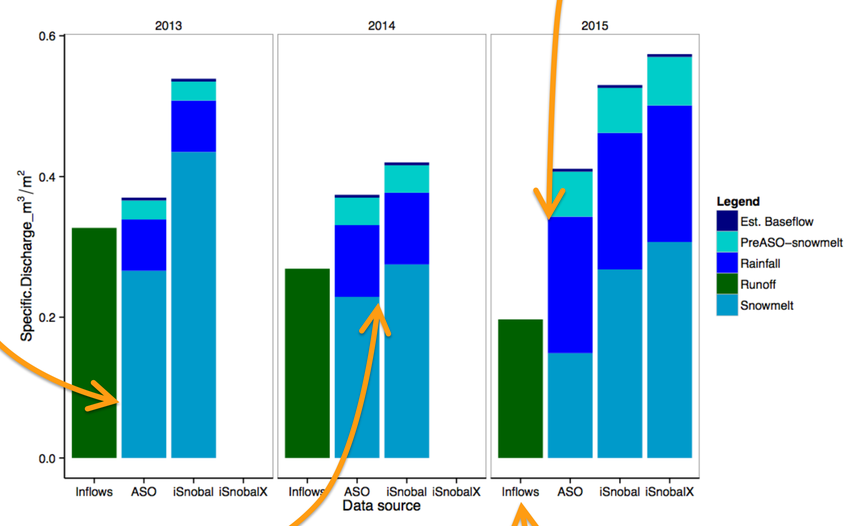

The model appears to be accumulating too much snow, which is largely a result of uncertainty in the precipitation forcing information.

Figure 8 – Annual water balance components from ASO, iSnobal and iSnobalX (a realization of the model after ASO snow depth data assimilation)

The year of 2015 was anomalously dry, in the already dry period since at least 2013, with 27-40% less runoff than 2013 and 2014.

Future work

- Continue to explore these water balance breakdowns using the ASO data for other basins in California and Colorado such as the Kings Canyon, Merced, Mammoth Lakes Basin, Rush Creek and the Uncompaghre.

Conclusions

- We knew that precipitation networks were largely inadequate at the basin scale. But, what we didn't know is how inadequate and in what ways. ASO provides data that can help address these questions.
- Unexpectedly, this work suggests that precipitation extrapolation techniques may be overestimating high altitude precipitation.
- With ASO-constrained snow water content, we can now begin to explore water balance features at the basin scale in areas that have been historically difficult to study due to uncertainty in precipitation fields, where this research forms an important step in the process during a considerable drought, when every drop counts.

3 McGurk Hydrologic, Orinda, CA, USA
4 Snow Hydrology Research Group WSL, Davos, Switzerland
5 National Snow and Ice Data Center, University of Colorado, Boulder, CO, USA

Poster No. EA-8

National Aeronautics and Space Administration

The 2014 California King Megafire: Synergistic applications of hypserspectral visual to shortwave infrared, multi-band thermal infrared, and LiDAR

E. Natasha Stavros (329c)
Supervisors: Dave Schimel (3290) and Simon Hook (3290)






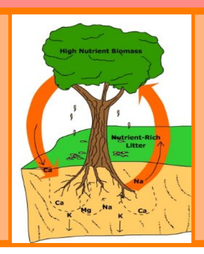


Background/Impact

- Megafires have huge and lasting ecological, social, and economic impact (Fig. 1)
- Unique climatology and behavior (Fig. 2), and a small sample size = unpredictable and difficult to manage for and during
- Megafire occurrence is increasing in the Western US (Table 1); thus, there is growing interest from the ecological and political communities about understanding megafires
- Because of the pre-HyspIRI airborne campaign and inter-agency collaborations between NASA and the US Forest Service, we have **unprecedented** remote sensing data from before and after the California King Fire (2014)
- These data can better characterize megafire behavior and impacts through time

Figure 1: (above) Fire impacts include risk to infrastructure, degraded air quality, toxic gases, hydrophobicity of soils, erosion and loss, nutrient cycle, changed ecosystem structure, and threat to endangered species.

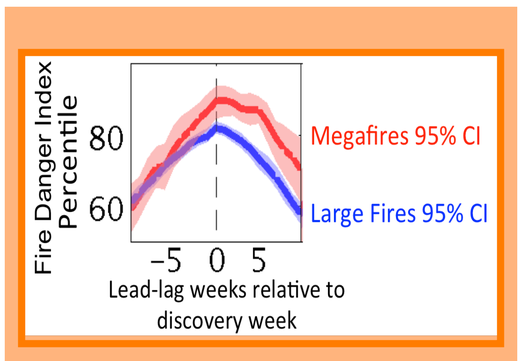

Figure 2: (above) Megafires in red have different fire potential and behavior than other large wildfires.

Table 1. Region	IPCC scenario	Likelihood of megafire for 2031-2060 compared to 1979-2010
Eastern Great Basin	RCP 4.5	2.054
	RCP 8.5	2.47
Northern California	RCP 4.5	1.353
	RCP 8.5	1.381
Northern Rocky Mtns.	RCP 4.5	1.531
	RCP 8.5	1.928
Pacific Northwest	RCP 4.5	3.136
	RCP 8.5	4.401
Rocky Mountains	RCP 4.5	4.694
	RCP 8.5	4.769
Southern California	RCP 4.5	1.499
	RCP 8.5	1.655
Southwest	RCP 4.5	*2.042*
	RCP 8.5	*2.024*
Western Great Basin	RCP 4.5	1.882
	RCP 8.5	1.951

Objective

Provide and assess high-level remote sensing data products from airborne campaigns that characterize megafire behavior and dynamics, in such a way that can inform fire management decision making both during and after such uncharacteristic events

Methods

1. Process Level 2-3 data products for Light Detection and Ranging (LIDAR), hyperspectral Airborne Visible/Infrared Imaging Spectrometer (AVIRIS), and multi-band thermal infrared imager (MASTER) (Fig. 4a; http://wildfire.jpl.nasa.gov) and validate spectral response (Fig. 5) by fire severity classification (Fig. 4b)
2. Develop "fuel model" maps (Fig. 6) that represents fuel amount, type, condition, and structure
   - Extrapolate pre-fire LiDAR from post-fire LiDAR (Fig. 4a) using quadratic regression (Table 2)
   - Spectral unmixing of AVIRIS into dominant vegetation types (Fig. 4c)
   - K-means unsupervised classification of LiDAR data
   - Crosswalk unique combinations of dominant vegetation and LiDAR classifications into fuel models (Fig. 6)
3. Compare MASTER thermal image (Fig. 4d) to heat flux output from a high spatial (123 m) and temporal (1 second) resolution fire behavior simulation model, Coupled Atmosphere-Wildland Fire Environment (CAWFE), which uses fuel model inputs (Fig. 7)

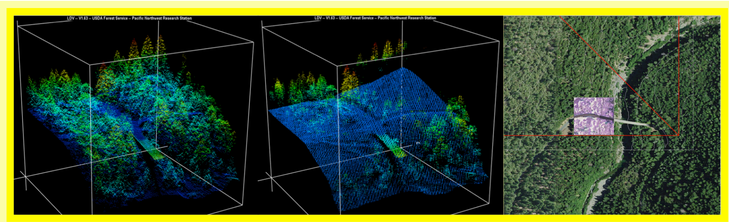

Figure 3: (Left) Difference in LiDAR, located in the Rubicon valley. point cloud from before and after the King Fire

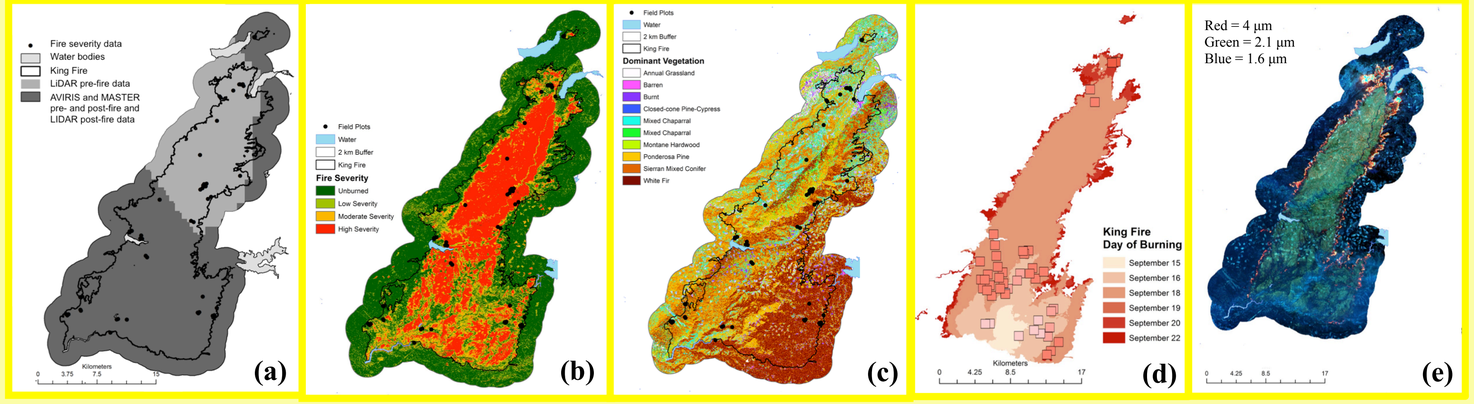

Figure 4. (a) Available data, (b) fire severity, (c) dominant vegetation, (d) MODIS active fire pixels (~1 km squares) on daily fire progression map, (e) MASTER September 19th, 2014 thermal image at 30 m resolution used for comparing CAWFE heat flux output

Results

Figure 5: MASTER and AVIRIS validation of post-fire spectral response shows consistent spectral response between instruments that responds to different fire severity ground observations with more pronounced spectral response patterns at higher fire severities

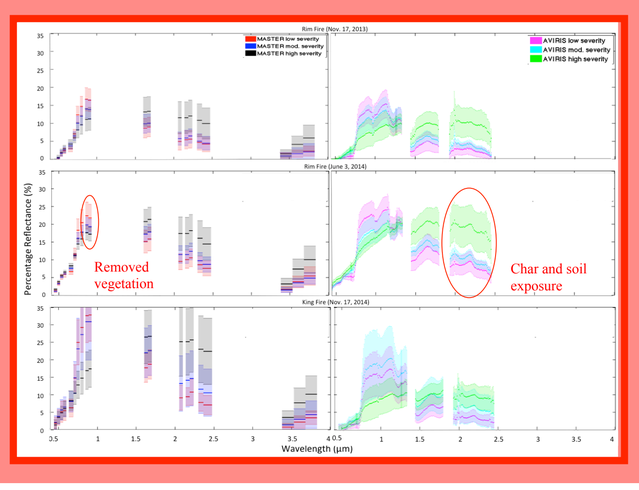

Table 2. Quadratic regression models where y = pre-fire LiDAR and x = post-fire LiDAR	R^2
standard deviation of LiDAR returns above 2 m	0.79
height of 95th percentile of LiDAR returns	0.86
heightof 25th percentile of LiDAR returns	0.53
percent fractional cover for returns above 2m	0.22

Post-fire LiDAR has a predictive relationship with pre-fire LiDAR, that varies only slightly by fire severity classification, thus a single model was used to extrapolate pre-fire LiDAR to the full fire extent for fuel model development

Figure 6: (a) AVIRIS-LiDAR fused fuel models are more current and uses more information to identify fuel models than the (b) LANDFIRE database developed using Landsat

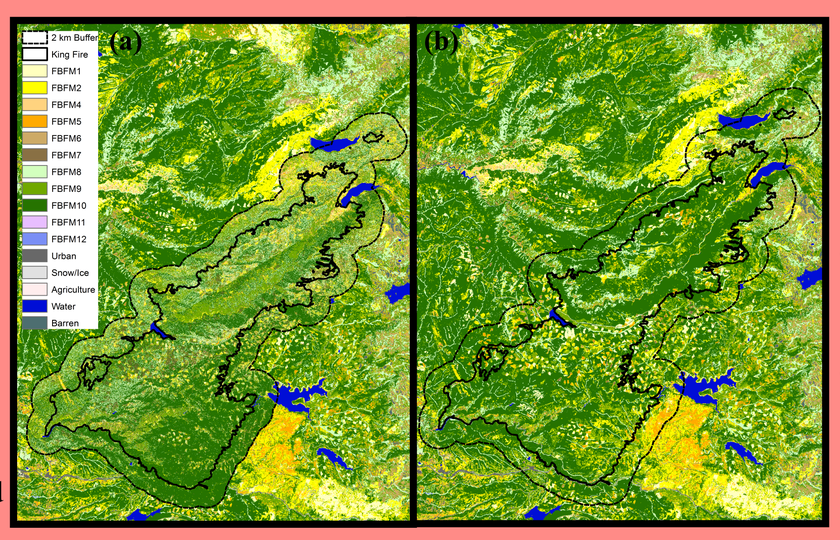

Figure 7: Successful CAWFE simulation of King Fire fire growth with the fuel model input

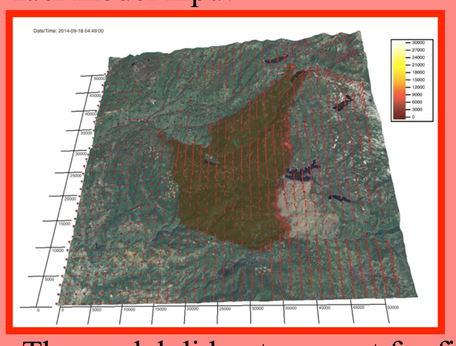

- The model did not account for fire retardant that was dropped on the Eastern edge
- The King Fire burned so hot it generated its own weather unique from nearby weather stations, thus it was not well simulated by fire behavior models that exclude this intrinsic fire-weather feedback

Conclusions and Future Work

- Megafire behavior differs from other wildfires in that megafires create their own localized weather that feeds back to its fire behavior and thus cannot be captured by current operational models
- Land resource managers are using these data to make post-fire decisions that protect people, infrastructure, and natural resources
- Future research will quantify: 1) the relationship between remote sensing fuel model classification and those assigned to forest inventory plots, 2) uncertainty maps, 3) carbon emissions from fire, and 4) the difference between CAWFE simulated heat release and MASTER measured heat release.

National Aeronautics and Space Administration
Jet Propulsion Laboratory
California Institute of Technology
Pasadena, California
www.nasa.gov

Poster No. EA-9

CL#15-3067

National Aeronautics and Space Administration

High-resolution remote sensing of water quality in the California Bay-Delta using the Portable Remote Imaging SpectroMeter (PRISM)

Principal Investigator: Cédric G. Fichot (329D)
David R. Thompson (382B), Michelle Gierach (329D)
Bryan Downing, Brian Bergamaschi, Lisamarie Windham-Myers, Mark Marvin-DiPasquale (USGS)

Introduction

The Bay-Delta is a major freshwater resource for California

- Largest watershed on west coast, confluence of Sacramento/San Joaquin rivers
- Supplies ~9 km^3 of water to California each year
- Supplied to 1 million hectares of farmland + 27 million people

The Bay-Delta is a highly altered ecosystem

- 120,000 hectares of tidal marshes reclaimed for agriculture
- Subsidence on levied islands
- Deterioration of habitats, biodiversity, and water quality

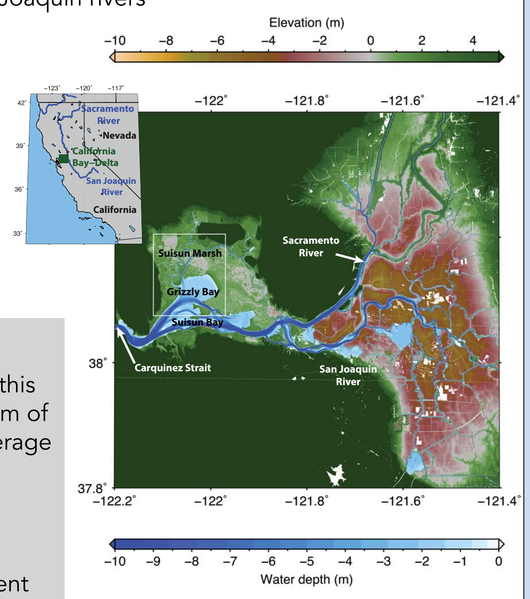

Problem:

The water quality monitoring that is critical to the management of this important water resource and ecosystem relies primarily on a system of fixed water-quality monitoring stations, but the limited spatial coverage often hinders understanding.

Objective:

Assess how hypersepctral imaging spectroscopy can enhance current water quality monitoring strategies and inform water management decisions.

Simultaneous retrieval of water quality indicators

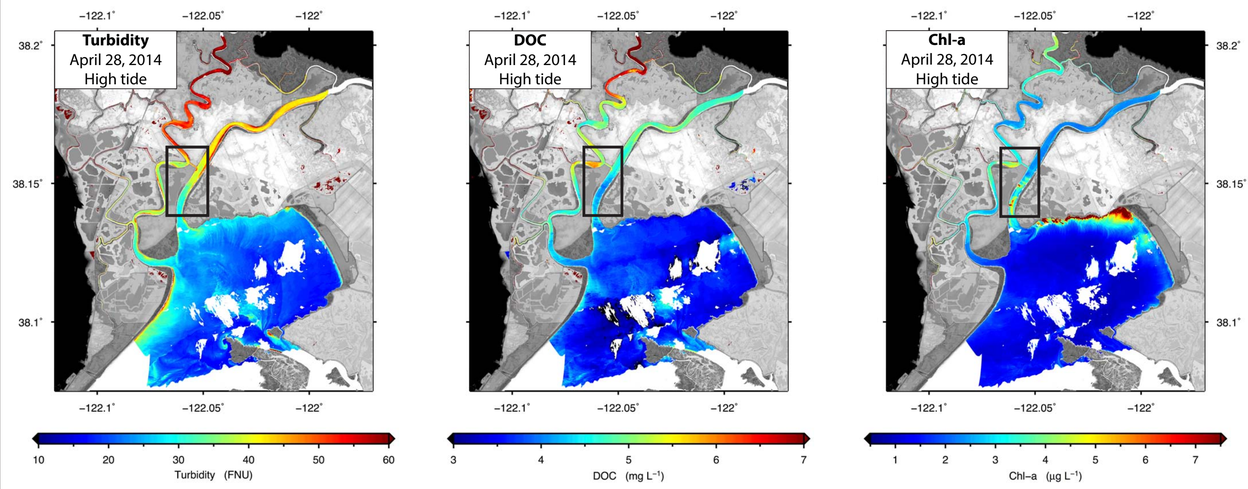

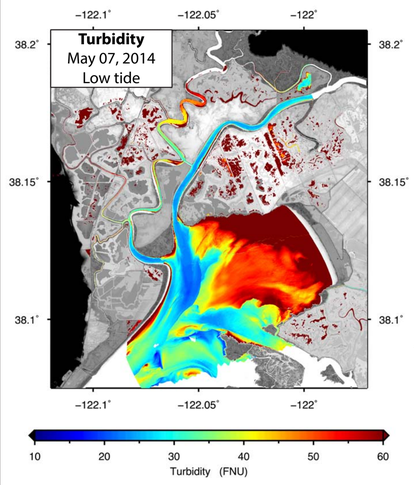

Spatial Resolution
2.6 x 2.6 m

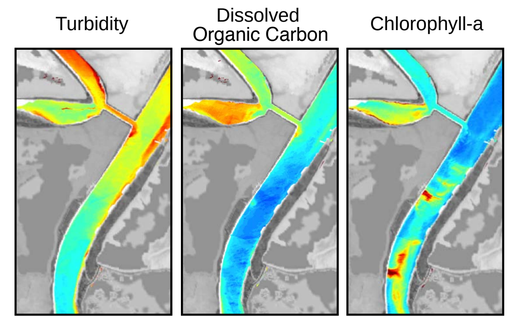

Applications of hyperspectral imaging spectoscopy for water quality in the Bay-Delta:

1) Remote detection of point- and non point-source pollution.
2) Understand the development and evolution of turbidity plumes, and its link to sediment transport.
3) Assess the impact of wetland restoration and climate-drive changes on water quality
4) Foster a better understanding of the factors regulating biological productivity in these waters.
5) Understand the factors driving the distribution of fish species like the endangered Delta smelt, which often interferes with water pumping operations and affects water-management decisions.

The Portable Remote Imaging SpectroMeter (PRISM)

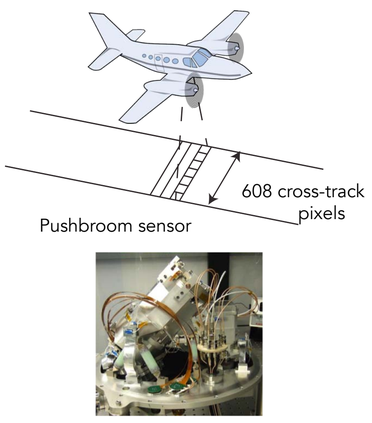

Spectral range: 350 - 1050 nm
Spectral sampling: ~ 3 nm
IFOV resolution : 0.97 mrad
Radiometric range : 0 - 99% R
Signal-to-noise at 450 nm: 500
Polarization variation: <1%
Spectral uniformity: > 95%

Mouroulis et al., *Applied Optics*, (2014)

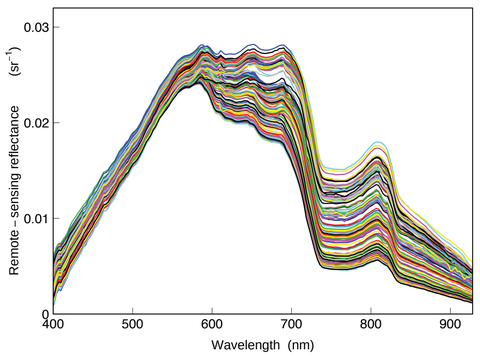

PRISM flyovers of Grizzly Bay, CA (April 28-29, 2014)

1) *In situ* water quality indicators (Turbidity, DOC proxy, Chl-a proxy) were collected underway during the PRISM flyovers using a custom-made flow-through system on a USGS watercraft.
The DOC and Chl-a proxies were calibrated against laboratory measurements.

2) The *in situ* water quality indicators and PRISM reflectances were matched in time and space.

3) Algorithms based on partial-least-squares regressions of the hyperspectral reflectances on the water quality indicators were developed using the April 28 data, and independently validated using the April 29 data.
The algorithms retrieved water quality values within a few % of the values measured *in situ*.

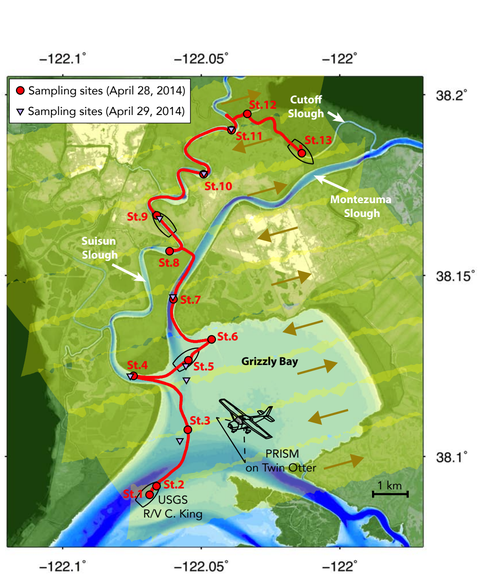

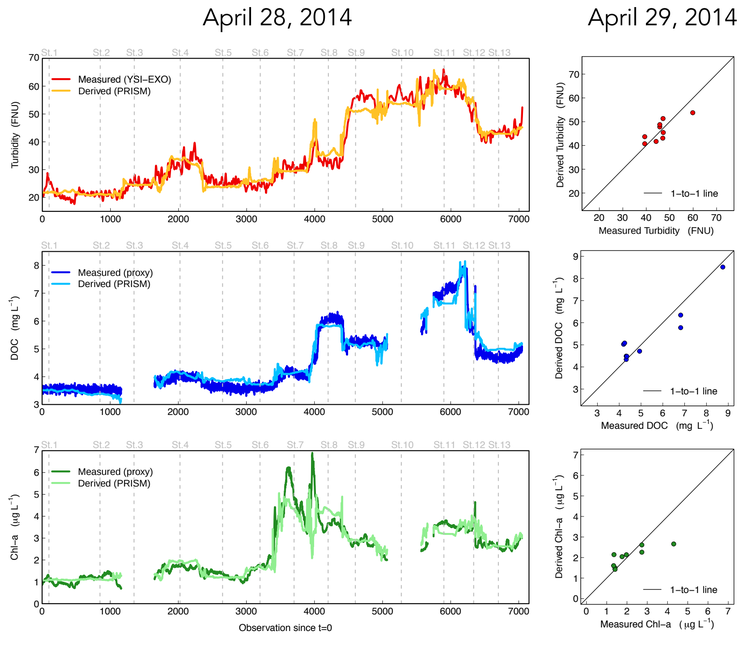

Remote sensing of methylmercury distributions

Methylmercury is a potent neurotoxin that bioaccumulates in living organisms.

Methylmercury binds strongly to DOC.

Methylmercury can be amenable to detection by remote sensing if the methylmercury-DOC relationship is well understood and constrained for a system.

Restored wetlands can act as a new source of DOC and methylmercury to surrounding waters.

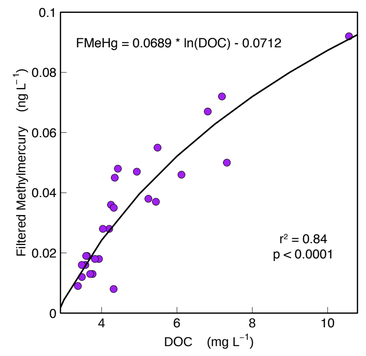

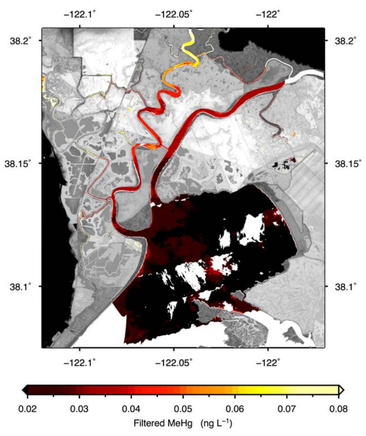

High-resolution imaging spectroscopy can help monitor and understand the effects of wetland restoration on the distribution of methylmercury and potentially of some important contaminants in the Bay-Delta.

Conclusions

1) We demonstrated the feasibility of accurately monitoring important water quality indicatorrs at high spatial resolution in the California Bay-Delta using the latest technology in hyperspectral imaging spectroscopy.

2) High-resolution, hyperspectral imaging spectroscopy can help inform management and policy development by facilitating the detection of point- and non-point-source pollution, and providing data to help assess the complex, diffuse impacts of wetland restoration and climate change on water quality and ecosystem productivity in highly dynamic and heterogeneous systems.

National Aeronautics and Space Administration
Jet Propulsion Laboratory
California Institute of Technology, Pasadena, California
www.nasa.gov

Poster No. EA-11

Monitoring and understanding seasonal and interannual variations of sea surface salinity associated with the Mississippi River plume

Séverine Fournier, Tong Lee and Michelle Gierach
Jet Propulsion Laboratory, California Institute of Technology, Pasadena, California, USA, section 329, email : severine.fournier@jpl.nasa.gov

National Aeronautics and Space Administration

MOTIVATION :

- **Large rivers** are key elements of the global **hydrologic cycle** and can influence **air-sea interactions** by modulating the vertical gradient of ocean density near the surface.
- Large rivers also provide organic and inorganic particulates into the ocean, **impacting biogeochemical and ecological activity**.
- The **Mississippi River** is **the largest river in North America** in terms of runoff. Therefore monitoring the spatial and temporal variability of the Mississippi River plume is important to biophysical interactions at local and regional scales.

- **WHAT :** Investigate seasonal and interannual variations of SSS
- **WHERE :** In the Mississippi River plume area of the Gulf of Mexico (GoM)
- **WHEN :** During 2010-2014
- **HOW :** SSS measurements from the Aquarius/SAC-D and SMOS missions

FRESHENING ASSOCIATED WITH THE MISSISSIPPI RIVER PLUME IN THE GoM :

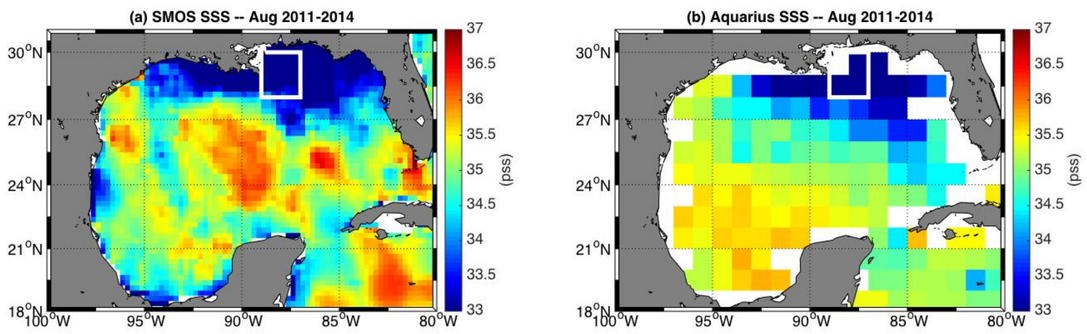

Fig 1 : Spatial SSS patterns in the GoM averaged over August for 2011-2014 from (a) SMOS and (b) Aquarius.

March-April : the Mississippi River **discharge** reaches a **maximum** (Fig 2c).

July-August : a **maximum freshening associated with the river plume** is clearly distinguishable from surrounding waters, extending from the river mouth (Fig 1).

SEASONAL AND INTERANNUAL VARIABILITIES AT THE MOUTH OF THE MISSISSIPPI RIVER :

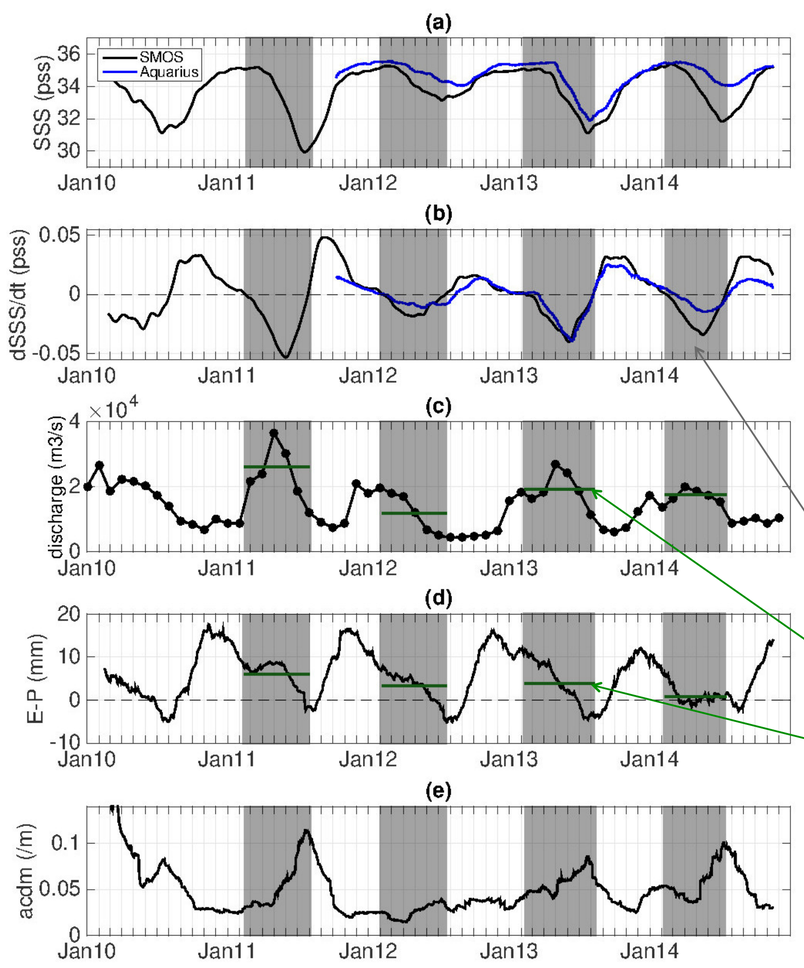

A **seasonal cycle** is clearly observed in SSS with a **magnitude** of ~**4 pss** (Fig 2a) and in acdm (Fig 2e).

Summer 2011 : the SSS signal is a record minimum, few months after the extreme Mississippi River flooding event.

Summer 2012 : highest SSS minimum (3 pss for SMOS SSS : **comparable to the magnitude of the seasonal variation**).

Fig 2 : 90-day running mean time series of (a) SMOS and Aquarius SSS, (b) SMOS and Aquarius SSS tendencies, (d) E-P and (e) acdm averaged within the white squares shown in Fig 1. (c) Monthly time series of Mississippi River discharge.

DOMINANT INFLUENCE OF RIVER DISCHARGE ON SEASONAL AND INTERANNUAL TIME SCALES :

Relationship between SSS tendencies, E, P and R at the mouth of the river :

$$dSSS/dt = (E-P) - R + \text{ocean dynamics}$$

- **Agreement** between the **SSS seasonal variations** and the **discharge** forcing.
- **Consistence** between the timings of the **SSS minimums** and **acdm maximums** (acdm used as a freshwater tracer).
- **Summer 2011 :** largest negative tendencies of SSS, largest river discharge but highest E-P.
- **Summer 2012 :** much smaller negative tendencies of SSS, smaller river discharge. And there is a lack of seasonal peak in acdm (freshwater tracer).

SUMMER 2012 MISSISSIPPI RIVER PLUME EXTENSION :

S**maller extension** of the Mississippi River plume in July 2012 than for other years (Fig 3).

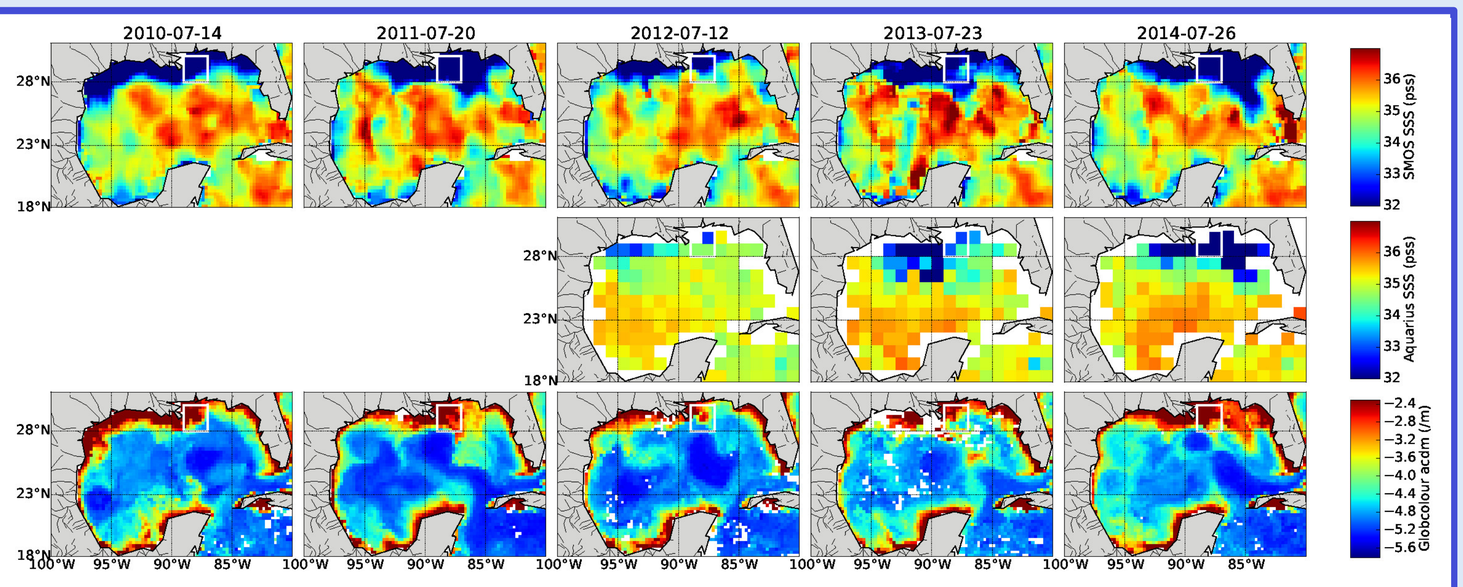

Fig 3 : SMOS SSS, Aquarius SSS and acdm maps during the 10-day periods when the SSS in the white square region reaches a minimum in different years. The time labels indicate the centers of these 10-day periods.

CONCLUSIONS :

- **Interannual changes** in the SSS minimum, **comparable to the magnitude of the seasonal cycle**, near the Mississippi River mouth.
- Seasonal **and interannual SSS variations consistent with the river discharge** variations, but not with **the E-P variations**.
- **Implications to ocean model simulation and forecast** : ocean models typically use climatological river runoff forcing and often relax SSS to climatology, suppressing interannual changes as observed.
- **Implications to marine ecosystems** (GoM : the largest hypoxic zone affecting the US) : satellite SSS measurements could be potentially used as one of the diagnostic quantities to monitor and predict the extent of hypoxic zone which depends on river discharge that modified the stratification, nutrient loads, weather conditions and ocean currents.

DATA :

Aquarius/SAC-D SSS : daily, 1° resolution (PO.DAAC)
ESA SMOS SSS : 10-day, 0.25° resolution (LOCEAN, CECOS/CATDS)
MERIS/MODIS/SeaWIFS acdm : daily, 4km resampled at 0.25° resolution (GlobColour)
ERA-Interim E and P : 3-hourly, 0.5° resolution
USGS monthly discharge data of the Mississippi River at the Baton Rouge gauge

National Aeronautics and Space Administration
Jet Propulsion Laboratory
California Institute of Technology
Pasadena, California
www.nasa.gov

Poster No. EA-12

National Aeronautics and Space Administration

Relative contributions of sea surface salinity and temperature to density gradient and tropical instability waves

Principal Investigator: Audrey HASSON (329D)
Tony LEE (329D)

MOTIVATIONS

Why do we study Density and its Meridional Gradient ?

- Density impacts directly the ocean dynamics
- Density gradient modulates the energy transfer between mean flow and eddies/waves, i.e. the baroclinic conversion of background available potential energy to the pertubation potential energy (PPE)
  - Associated with the generation and propagation of tropical instability waves (TIWs)

The meridional surface density gradient is modulated by both the surface Salinity and Temperature

- The effect of surface salinity (SSS) contrasted with temperature (SST) has not been evaluated for both the Pacific and Atlantic Oceans

OBJECTIVES

- Spatial variations of SSS & SST gradients and their relative contribution to density gradient.
- Intraseasonal variability of SSS, SST and thus density gradients
- Relationship of the background density gradient to TIW-related density variability
- Consistency among different datasets

1. SEA SURFACE DENSITY (Mean, Variability and Gradient)

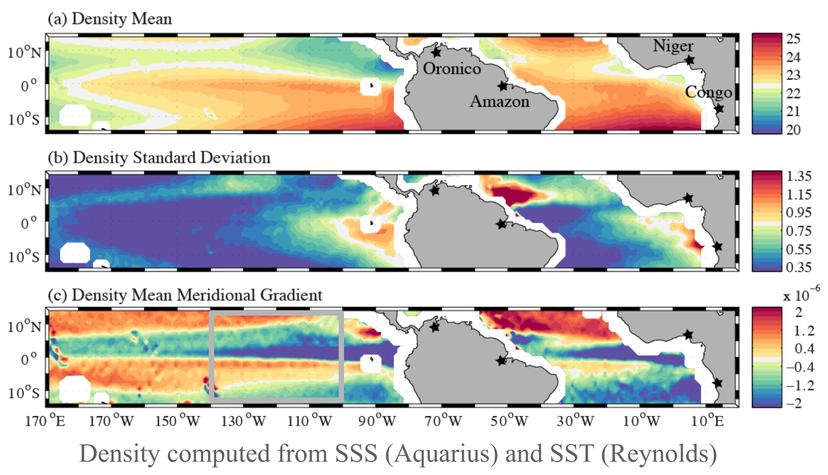

Density computed from SSS (Aquarius) and SST (Reynolds)

- **High Density** in the upwelling systems
- **Low Density** in the Intertropical Convergence Zones (ITCZ)
- **Strongest Variability and Meridional Gradient** near the river outflows
- **HighVariability and Meridional Gradient** in the ITCZ and equatorial cold tongue

2. Mean SSS, SST and Density MERIDIONAL GRADIENTS

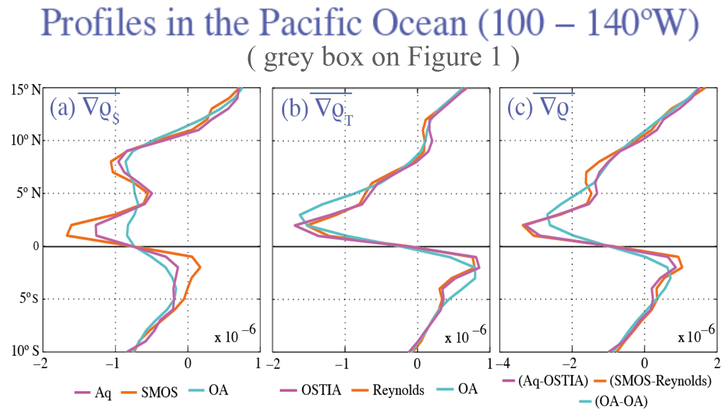

Salinity $\nabla\rho_S = \beta \cdot \nabla SSS$

Temperature $\nabla\rho_T = -\alpha \cdot \nabla SST$

Density $\nabla\rho = \nabla\rho_S + \nabla\rho_T$

- **Steep Narrow Fronts** around the equatorial upwelling
- **$\nabla\rho_T$ is Anti-symetrical** across the equator
- **$\nabla\rho_S$ has a Second Maximum** in the vicinity of the ITCZ
- On the equator **$\nabla\rho_S$ is 6.2 times greater than $\nabla\rho_T$**
- **Coherent structures** between the different products
- **Observations-based product (green)** does not represent adequately the $\nabla\rho_S$

3. INTRASEASONAL VARIABILITY of the Density Gradient

- **High Density Variability** found within 2° of the equator contributed by **both SSS and SST**
  - Linked to the presence of **TIWs**
- **Density Variability** near the major outflows and North of the Equator **mainly due to SSS**
  - Because of fresh water input from land and the atmosphere

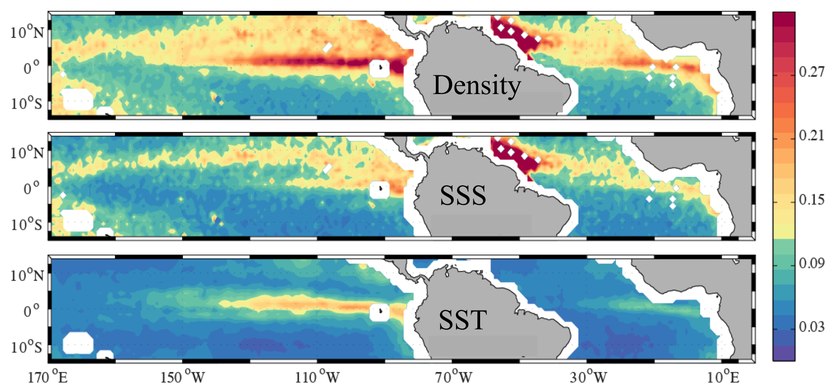

Standard Deviation of the gradients of Density, SSS (Aquarius) and SST (Reynolds) filtered between 14 and 50 days

4. Link between PERTURBATION and BACKGROUND gradients

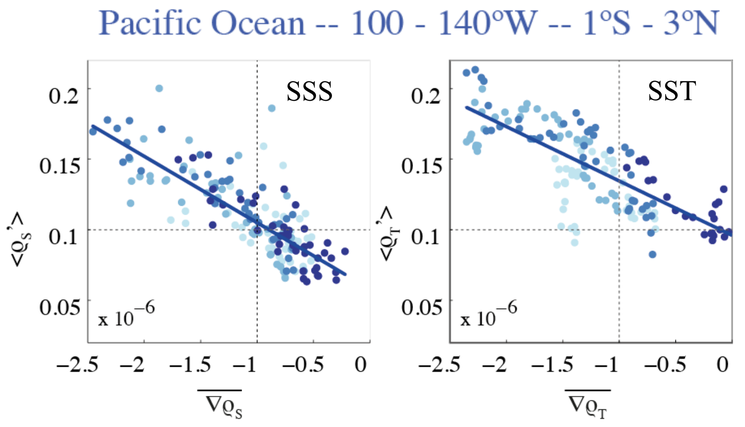

Slope = -47.2 km (R^2=0.64)

Slope = -38.7 km (R^2=0.68)

- The **near linear relationship** reflects the influence of the background gradient on its variability
  - i.e. the efficency of the **baroclinic conversion** of energy
  - Slopes suggest the isocontours displacement associated with the TIWs
- The **Atlantic Ocean** show stronger relations
- The **satellite based products are coherent**

5. Direct and Indirect CONTRIBUTIONS of SSS and SST to PPE

$$PPE \propto \underbrace{\overline{\rho'^2}}_{A} = \rho_0{}^2 \left(\underbrace{\overline{\rho_T{}'^2}}_{B} + \underbrace{\overline{\rho_S{}'^2} + 2\overline{\rho_S{}' \cdot \rho_T{}'}}_{C} \right)$$

(A) PPE Proxy

(B) SST Direct Contribubtion to the PPE Proxy

(C) SSS Total Contribution to the PPE Proxy

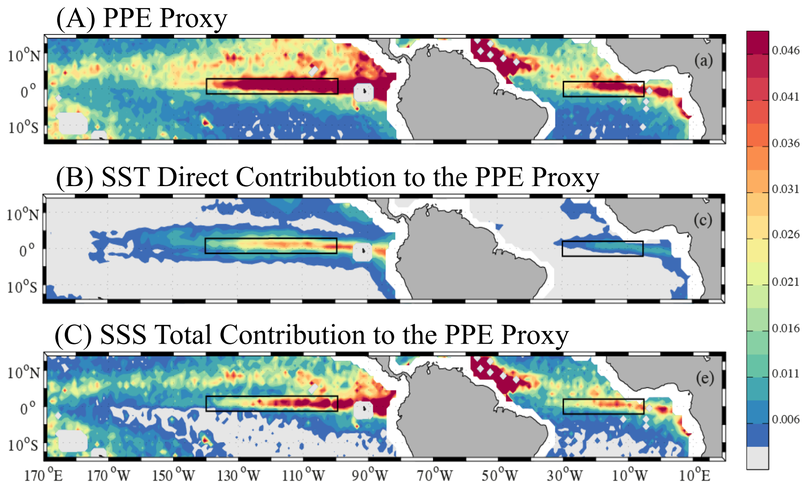

- **Baroclinic Conversion** of available potential energy from the background **is described by PPE**
- **Density Variance** can be used as a proxy as TIW-related variability is confined to the Mixed Layer
- **The Atlantic PPE is weaker by 22%** than the Pacific
- **Omitting SSS would lead to an underestimation of the PPE of**
  - 55% in the Pacific TIW region
  - 80% in the Atlantic TIW region
  - 86% in the Pacific ITCZ
  - 95% near the Amazon mouth

CONCLUSIONS AND FUTURE WORK

- **Aquarius and SMOS** derived SSS datasets are used to investigate the **SSS contribution to Density gradient and variability relative to the SST contribution**
- **Near 2°N** where the TIW are the most energetic, the mean density gradient is controlled by SSS and SST with comparable contributions
- **SSS controls the mean Density gradient** on the equator, under the ITCZ and near the river outlfows
- Different proxies reveal latitude-dependent region where **baroclinic** and/or **barotropic energy conversion** and/or **air-sea fluxes** control the **intraseasonal density variability**
- **Direct contributions of SSS and SST to the 14-50d density variability are of the same order of magnitude**. However, the contribution of both parameters to the density variance (a proxy for PPE and baroclinic conversion rate) is not equivalent
- **Omitting SSS would lead to an underestimation of the variance of 72%** over the tropical Atlantic and Pacific Oceans (thus PPE and baroclinic energy transfer by a factor of ≈3).
- **Future work includes the examination of the influence of the vertical structure of density on the baroclinic conversion and the respective influences of Salinity and Temperature**

DATASETS

- Aquarius/SAC-D satellite (NASA and the Argentinian Space Agency Comision Nacional de Actividades Espaciales) – Aq
Gridded 1 degree spatial resolution SSS from combined ascending and descending passes averaged over 7 day
+ V3.0 Level 3 product (Lee et al., 2012)

- SMOS satellite (2nd Earth Explorer Opportunity Mission of the European Space Agency- ESA) -- SMOS
Gridded ¼ degree spatial resolution SSS from combined ascending and descending passes averaged over 10 day

- SST Optimal Interpolation from the NOAA/National Climatic Data Center (Reynolds et al., 2007) – Reynolds
Gridded ¼ degree spatial resolution Daily OI SST from combined datasets (Ship, Buoy, AVHRR: NOAA19, METOP, NCEP-ice) V2.0

- SST Optimal Interpolation from the UK Met Office (Operational Sea Surface Temperature and Sea Ice Analysis – OA)
Gridded 0.054 degree spatial resolution Daily OI SST from combined datasets (AVHRR, AATSR, SEVIRI, AMSRE, TMI and in situ data from drifting and moored buoys) V1.0

- In Situ SSS and SST Objective Analysis from the Ifremer (In Situ Analysis System – OA)
Gridded ½ degree spatial resolution OA SSS and SST from combined datasets(Argo, TAO-TRITON moorings, CTD cast, marine mammals etc…) V.6

National Aeronautics and Space Administration
Jet Propulsion Laboratory
California Institute of Technology
Pasadena, California

www.nasa.gov

Poster No. EA-13

National Aeronautics and Space Administration

On the joint use of tracer images and altimetric fields to improve the assessment of the ocean surface

Principal Investigators: Lucile Gaultier (section 329D)
Lee-Lueng Fu (section 3200)
Jet Propulsion Laboratory, California Institute of Technology

CONTEXT

➢ Submesoscale and mesoscale dynamics play an important role in setting frontal structures in the upper layers of the ocean.
➢ Submesoscale filaments can be observed using high resolution (**HR**) tracer sensors (daily sea surface temperature (SST) or ocean color image, with a 1 km resolution) provided that the area is cloud free: few images are available.

➢ Low resolution (**LR**) microwave SST images and low resolution altimetric velocities are available daily with a resolution of 0.25^o.
➢ Dynamics and tracers are well correlated in some areas: Benefit from the synergy between velocity and tracer to improve the assessment of the ocean surface.

How to complement HR tracer images using Lagrangian advection of LR tracer observation and LR altimetric data?

METHODS

HR tracer images are computed using LR tracer images and LR velocities as mesoscale and submesoscale patterns can be inferred from large scale dynamics (Despres et al. (2011)). Two methods are tested:

1. **Advection alone** (option **A**): Backward Lagrangian advection of particles.
2. **Advection + nudging** (option **AN**): Backward Lagrangian advection of particles with nudging to a daily LR tracer observation to simulate source, sink and diffusion.

VALIDATION USING A MODEL

➢ MODEL DATA: data were produced by the Regional Ocean Modeling System (ROMS) off the Oregon coast by Dr. Yi Chao and his team. Initial spatial resolution of the model is 0.75 km x 0.56 km.
➢ ADVECTION DATA:

- Initial LR tracer image: SST filtered at 25 km
- Simulated observation: 'Altimetric' velocity (velocity degraded at 23 km), 'Microwave' SST (SST degraded at 25 km).

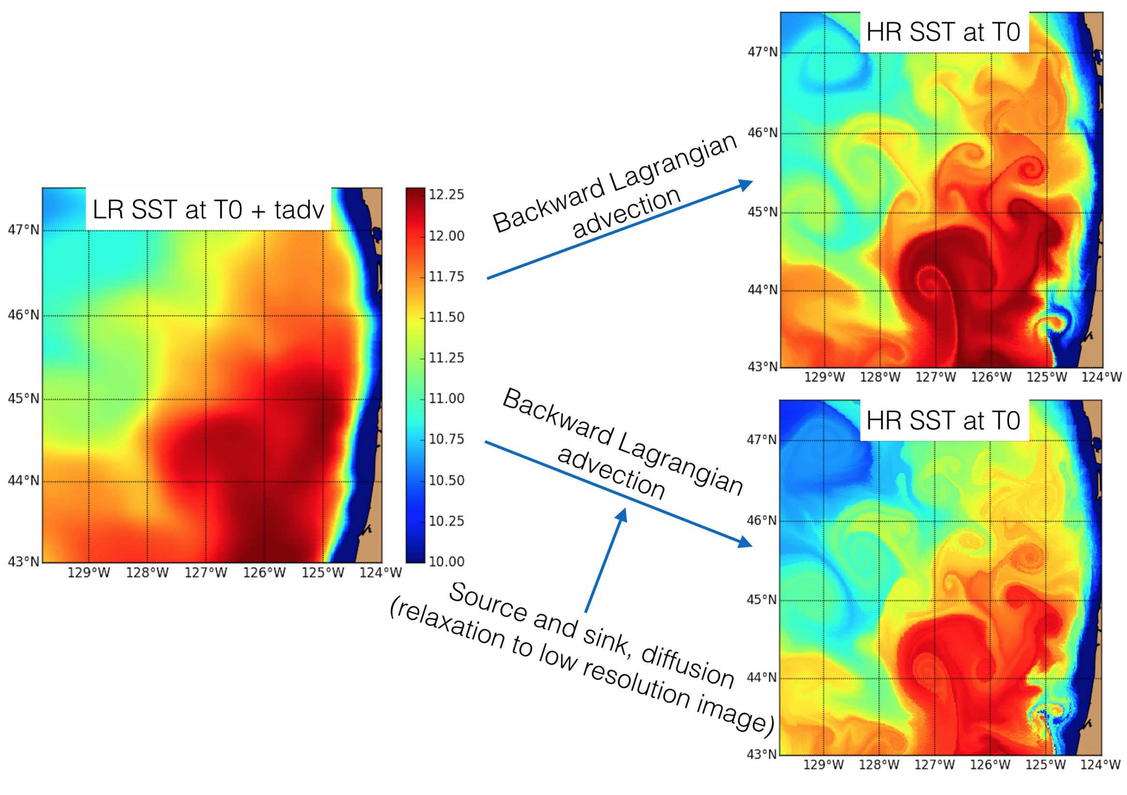

➢ SST is advected backward for 10 days using time-evolving 'Altimetric' velocities for option A and with a daily nudging to the LR 'Microwave' SST (option AN).

Comparison of advected SST with the truth from the model at T0

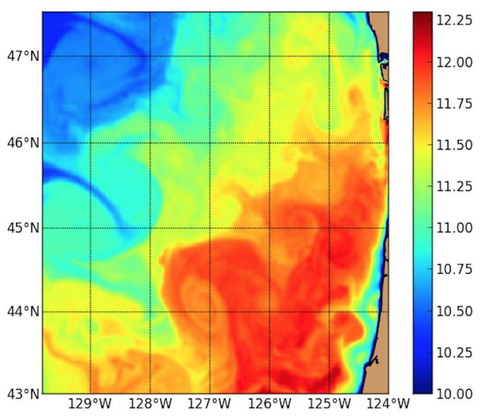

➢ Most patterns have similar shape and location to the truth in both advected tracer images.
➢ Filamentations look more realistic on the tracer image resulting from the advection of the tracer with the nudging than on the one resulting from the advection alone.
➢ Nudging to the LR SST observation acts as source and sink.

COMPARING THE TWO METHODS

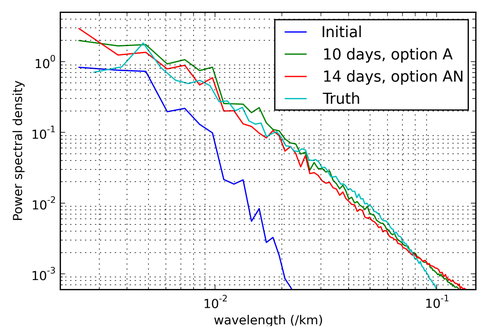

Power Spectrum Density of the SST for different types of advection (log-log scale)

➢ Spectrum slopes similar to the one in the model are reached after 10 days for option A (consistent with Dencausse et al. (2013)) and 14 days for option AN.
➢ Nudging (option AN) acts as diffusion: longer advection times required to fit the spectrum slope of the truth.

TEST CASE: REAL OBSERVATION

A small area in the South Atlantic ocean is chosen to perform some tests as interesting patterns are shown in HR Infra-Red SST images (cloud-free days, small scale dynamics).

➢ ADVECTION DATA:

- Initial tracer image: LR SST from AMSR, interpolated at the final resolution grid on 2012/10/28
- Velocity: AVISO daily mapped velocity ($0.25^o \times 0.25^o$)
- Nudging: Microwave daily SST from AMSR ($0.25^o \times 0.25^o$).

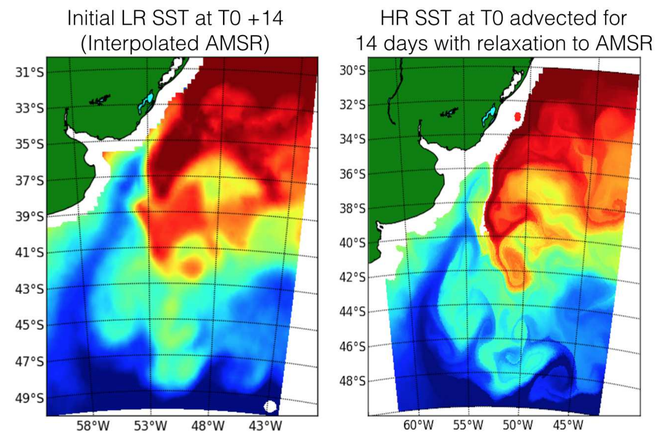

LR AMSR SST advected backward for 14 days using option AN (nudging to AMSR).

➢ The final advected HR SST field is compared with :

- HR MODIS daily observation ($0.04^o \times 0.04^o$) on 2012/11/11
- LR AMSR daily observation ($0.25^o \times 0.25^o$) on 2012/11/11

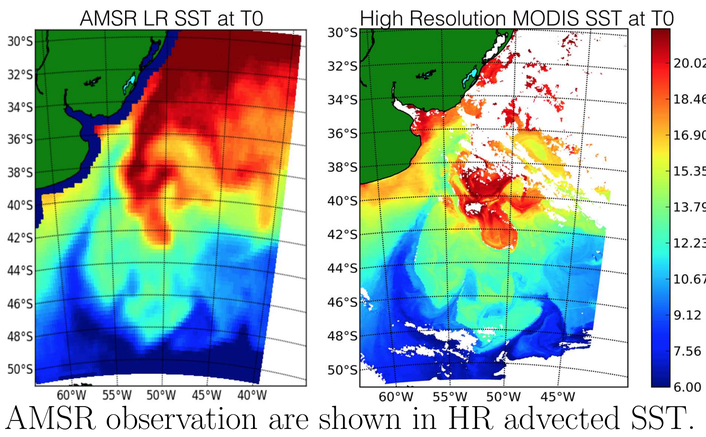

➢ Small patterns not visible in LR AMSR observation are shown in HR advected SST.
➢ Most patterns are similar in shape and location to the one visible in MODIS.

CONCLUSION AND PERSPECTIVES

HR tracer images computed from advection of LR tracer images using LR velocities are consistent with HR observations.

➢ 10 to 14 days of advection is needed to create small scale filaments depending on the chosen method.
➢ The most reliable method is the Lagrangian advection with a nudging to LR tracer images (option AN).
➢ Many applications arise from the computation of HR tracers using advection:

- Reconstruction of missing HR observation under clouds.
- Forecast of HR tracer in real time to detect eddies during a sea campaign.
- Eddy tracking: analyze the evolution of physico-biogeochemical surface properties of the water masses trapped into large eddies.

References

Dencausse, G., Morrow, R., Roge, M., Fleury, S., 2013. Lateral stirring of large-scale tracer fields by altimetry. Ocean Dynamics 64, 61–78.
Despres, A., Reverdin, G., d'Ovidio, F., 2011. Mechanisms and spatial variability of mesoscale frontogenesis in the northwestern subpolar gyre. Ocean Modelling 19 (1-2), 97–113.

National Aeronautics and Space Administration
Jet Propulsion Laboratory
California Institute of Technology
Pasadena, California
www.nasa.gov

Poster No. EA-14

National Aeronautics and Space Administration

The imprint of high sea winds in the extratropics on oceans

Yi-Hui Wang (329) and W. Timothy Liu (329)

Frequent strong ocean winds in the Northern Hemispheric extratropics are observed in boreal winters, which are closely linked to mid-latitude storms. What are the effect of frequent strong winds on oceans?

Objectives

This study investigates the imprint of frequent high winds on oceans using multiple observations during boreal winters (Dec-Jan-Feb).

Data

- CCMP surface wind speed in DJF of 1987-2010 at 0.25º grid; QuikSCAT in DJF of 1999-2008.
- OA-Flux at 1º grid.
- NOAA OI sea surface temperature (SST) at 1º grid.
- Ishii ocean temperature at 1º grid for ocean heat content.
- Aviso sea surface height (SSH) at 0.25º grid in DJF of 1993-2010.

Methods

- High wind occurs when daily mean wind speed exceeds 20m/s pointwise.
- High wind frequency: days of high wind in one month/number of observations per month.
- Area mean of high wind occurrences within identified frequent high wind regions.
- Apply correlation analysis to link area-mean high wind occurrences and temporal anomalies of oceanic variables without ENSO signals. No time lag is considered.

high wind occurrences averaged over one region

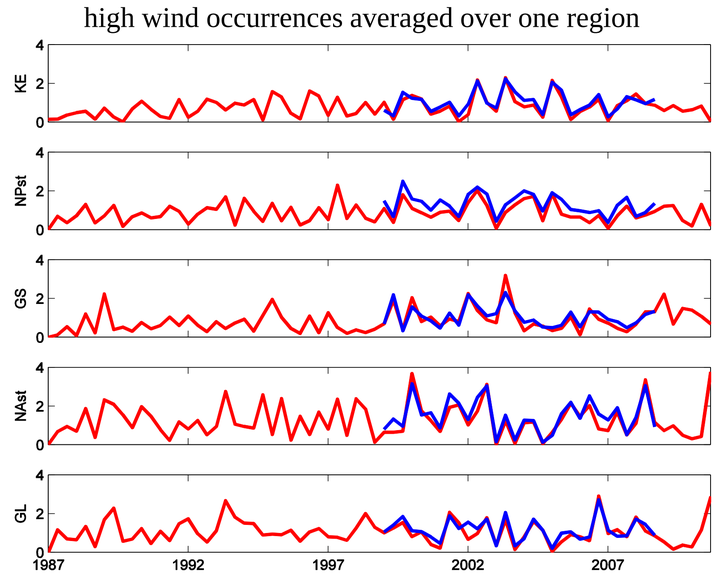

Red: CCMP
Blue: QuikSCAT

Frequency of high winds based on CCMP data

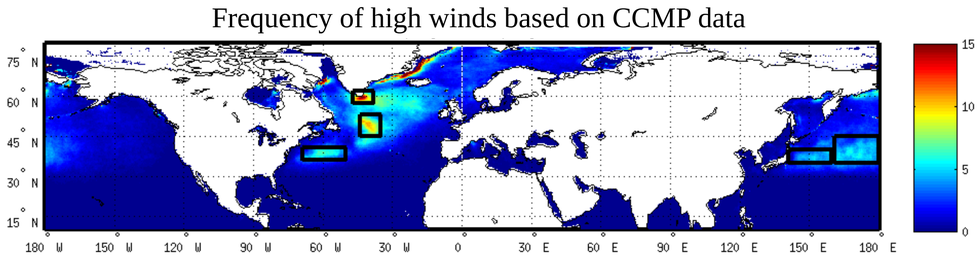

Maps of correlation coefficients between area-mean high wind occurrences and ocean variables

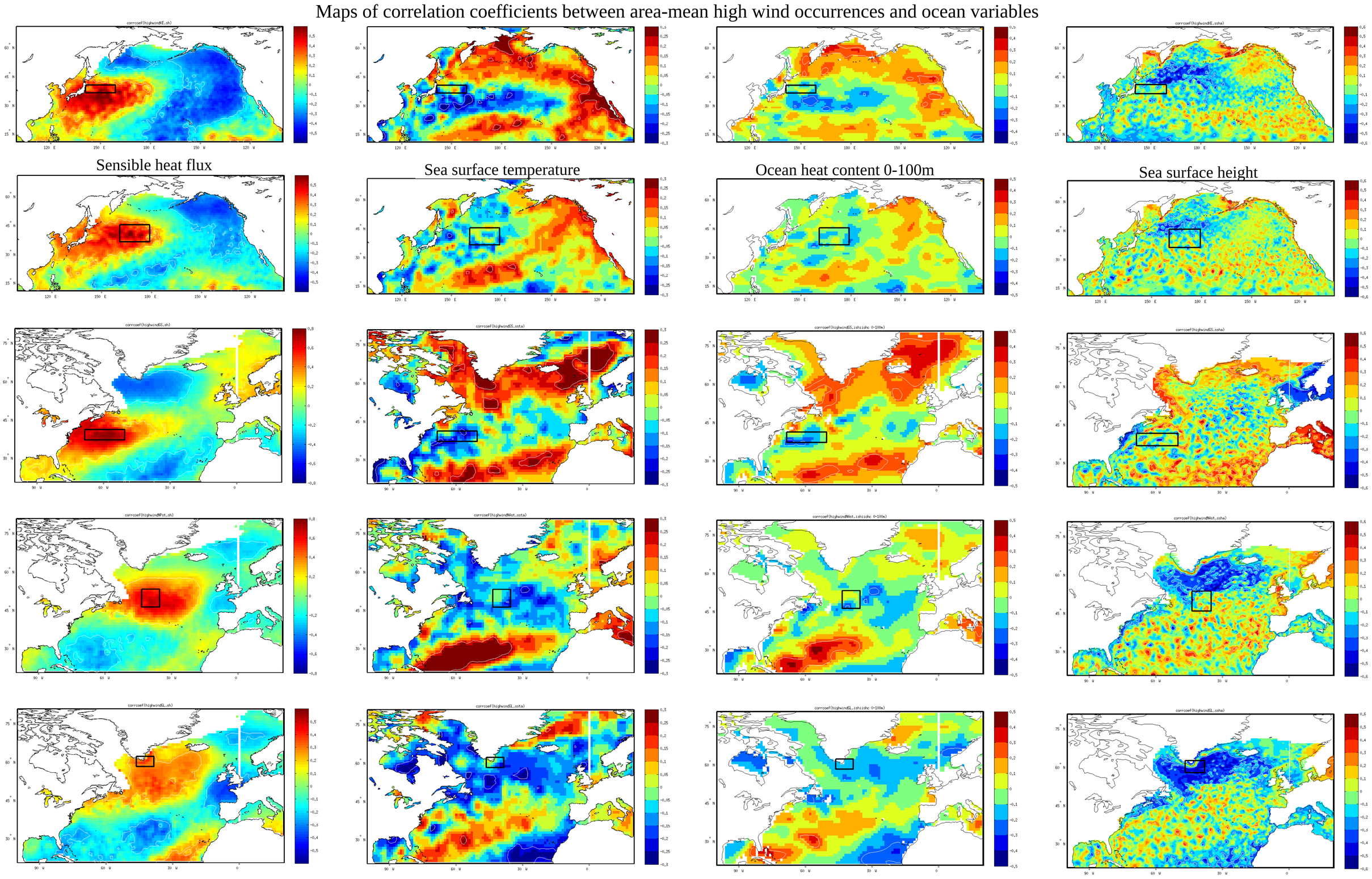

Results

- Five regions in the Northern Hemispheric extratropics are identified to display frequent high winds in boreal winter.
- CCMP data provide consistent variability of high wind occurrences with QuikSCAT data, despite that QuikSCAT data give slightly stronger wind speed.
- Month-to-month variability of high wind occurrences appears correlated with local surface heat flux, with SST, with ocean heat content, and with SSH to some degree. Frequent high winds generate regional heat flux release from the oceans to the atmosphere, which leads to cooler SST, less ocean heat content in near-surface layers and lower SSH. Weaker and opposite responses in the vicinity of strong responses suggest that the anomalous heat induced by frequent high winds is balanced.
- The effect of frequent high winds on the deeper oceans is unclear and will be studied in the future.

Poster No. EA-15

National Aeronautics and Space Administration

Jet Propulsion Laboratory
California Institute of Technology
Pasadena, California

www.nasa.gov

Acknowledgment: we want to thank Dr. Ichiro Fukumori for useful suggestions and the support of the NASA postdoctoral fellowship for this study.

National Aeronautics and Space Administration

GRACE observes Overturning Circulation in the Atlantic Ocean

Katrin Bentel (329F), Felix W. Landerer (335N), Carmen Boening (329F)
Mike M. Watkins (3200), David N. Wiese (392R)

1 Background & goal

- Atlantic Meridional Overturning Circulation (**AMOC**) is a key mechanism in basin-scale heat transport
  -> temporal variations indicate regional and global climate
- In-situ observations are sparse & AMOC is not coherent across the ocean basin

The new JPL-mascon release of GRACE gravity data provides the first high enough resolution to monitor AMOC variability by satellite gravimetry!

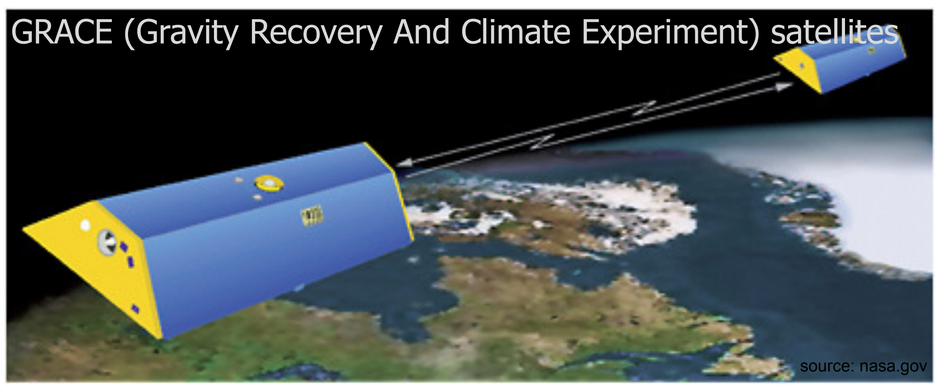

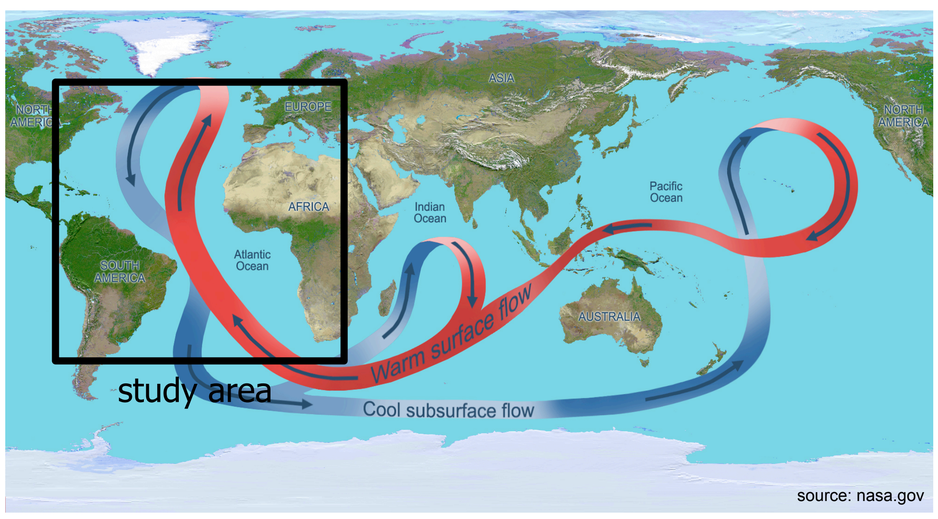

2 Method

AMOC (Ψ) is derived from ocean bottom pressure (**OBP**) at the basin boundaries (for each latitude y and depth layer dz)

$$\Psi(y,z) = \frac{1}{\rho_0 f}\int_{z_1}^{z_2}(OBP_E - OBP_W)dz$$

$$\rho_0 f = \text{const}$$

Atlantic cross-section: northward view (at lat *y*)

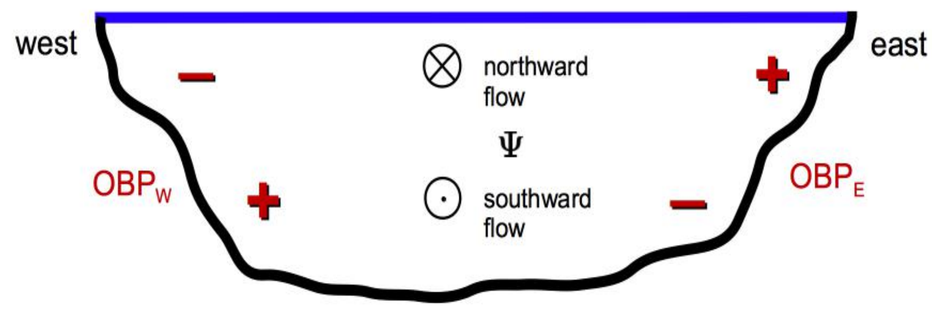

- North- and southward transport manifests in OBP differences at the eastern and western boundaries
- OBP anomalies are observed by GRACE

3 Data

GRACE JPL-RL05M mascon solution:

gravity data inverted for OBP,
best spatial resolution (3° mascons)

- AMOC not coherent across latitudes
- Signal concentrated on Western boundary in North Atlantic
- Steep bathymetry gradients (e.g., 1000 to 3000 m depth) difficult to resolve by GRACE => focus on deep layer with less steep bathymetry

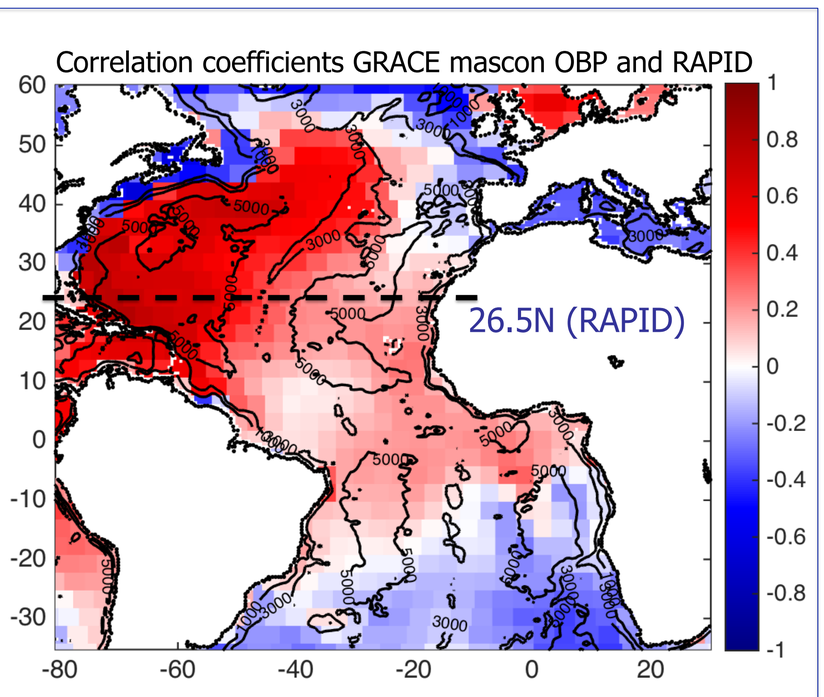

4 Results

AMOC is only fully observed by in-situ observations at latitude 26.5 N with an ocean-spanning hydrographic array of vertical profiles (**RAPID**)
Validation: Integrated transport from GRACE-OBP versus RAPID observations at 3000 – 5000 m depth:

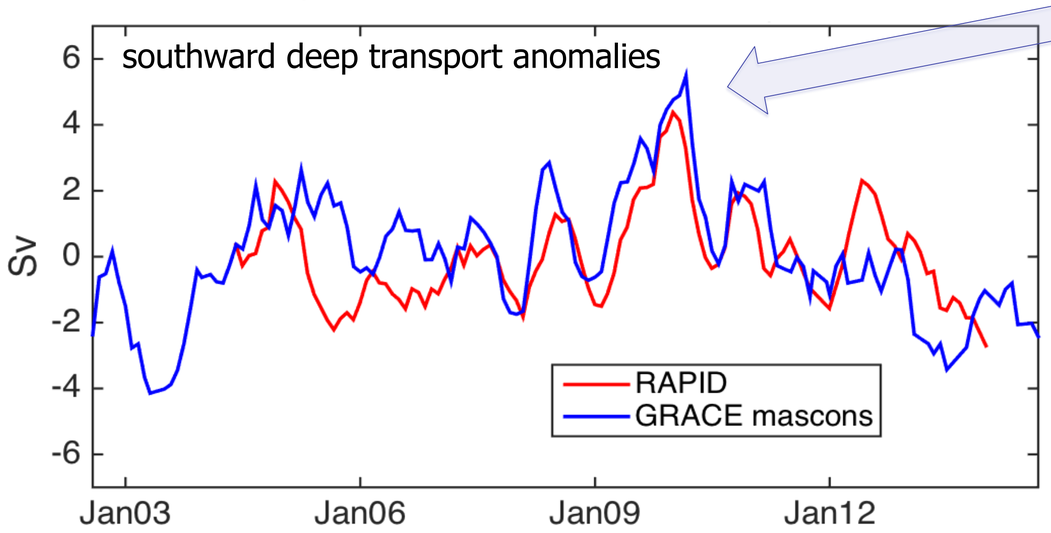

Positive southward transport anomaly (i.e. AMOC slowdown) in 2009/2010 has contributed to severe winter conditions in NW Europe and an intense hurricane season in summer 2010

- **Red** curve: in-situ observations (ship based or moorings)
  drawback: spatially limited (e.g., only at 26.5N spanning the ocean basin)
- **Blue** curve: derived from satellite gravimetry
  -> 13+ yr time series with *global* coverage
  drawback: spatial resolution
  solution: focus on deep layer (less steep bathymetry; can be resolved by GRACE)

5 Summary

- This is the first time satellite gravimetry has been used to monitor AMOC variability!
- AMOC transport (in the deep layer) is computed from GRACE-OBP data all across the Atlantic ocean and for the GRACE time period (2002 – present); verified at 26.5N (where in-situ observations are available)

National Aeronautics and Space Administration
Jet Propulsion Laboratory
California Institute of Technology
Pasadena, California

www.nasa.gov

Poster No. EA-17

National Aeronautics and Space Administration

Observing Large Megathrust Earthquakes From Space

Principal Investigator: Yuning Fu (335N)
Richard Gross (335N), Zhen Liu (329A), Tony Song (329E) and Felix Landerer (335N)

Introduction and Objective

Large destructive megathrust earthquakes occur at convergent plate boundaries where one tectonic plate subducts beneath another plate. Megathrust earthquakes are powerful with large magnitude In this study, we analyze spatial geodetic observations to measure different signatures of historical large megathrust earthquakes.

- **Gravity Recovery and Climate Experiment (GRACE):** detect the coseismic gravity change.
- **Global Positioning System (GPS):** Slow Slip Event (SSE) at southcentral Alaska subduction zone.
- **Real-time GPS**: fast determine coseismic displacement for Tsunami early warning.

Coseismic Gravity Change

Within a megathrust earthquake, the coseismic gravity change includes two components:

I. Mass redistribution inside the solid earth [Chao and Gross, 1987].
II. Ocean mass redistribution due to bathymetry change. [Broerse et al. 2011, 2014]

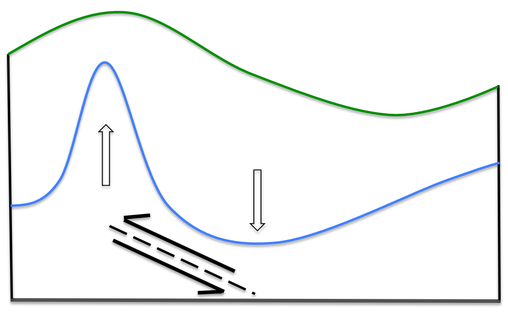

From:
Broerse et al. [2014]

Cartoon description how the bathymetric deformation due to a megathrust earthquake can change the geoid (and gravity). The figure is from Broerse et al. [2014].

2011 Tohoku earthquake
Coseismic rupture model: We et al. [2012]

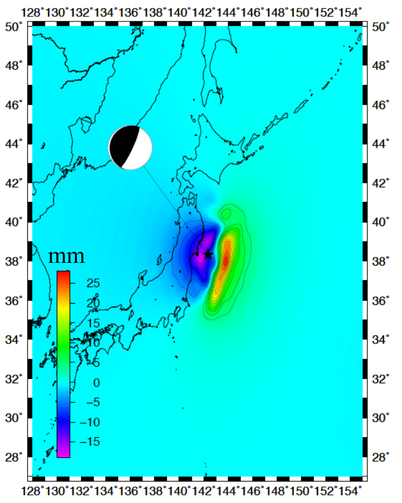

Geoid change due to the mass redistribution of solid earth. Degree/order up to 450.

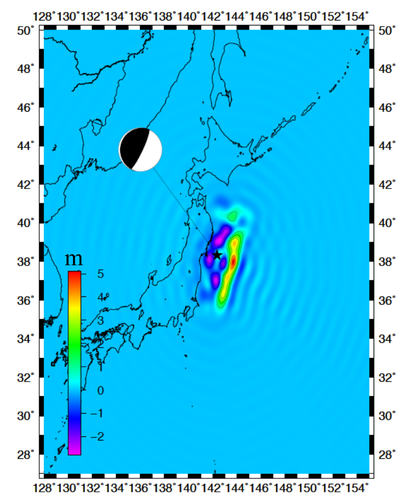

Bathymetry deformation of the earthquake.

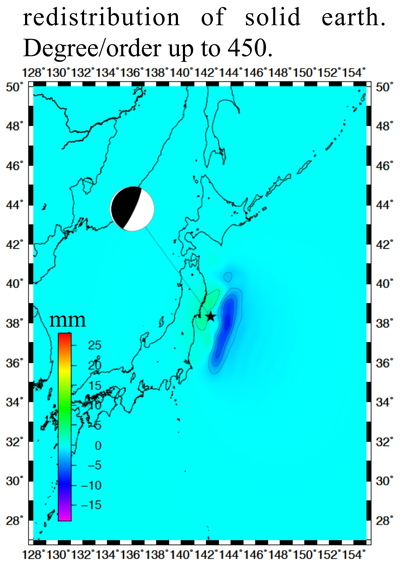

Geoid change due to ocean redistribution.

Total geoid change: solid earth effect + ocean redistribution effect.

National Aeronautics and Space Administration
Jet Propulsion Laboratory
California Institute of Technology
Pasadena, California

www.nasa.gov

GRACE: Coseismic Gravity Change

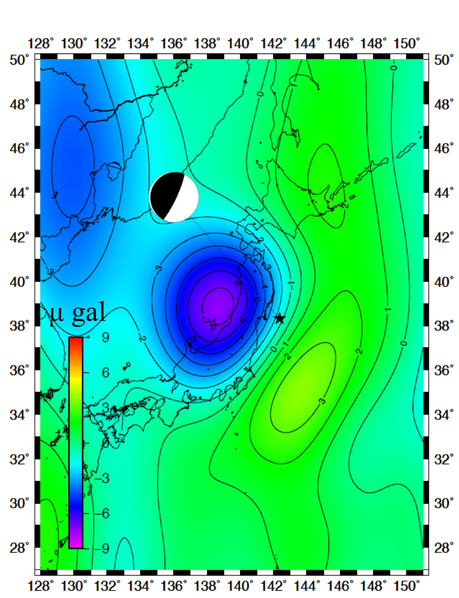

GRACE measured coseismic gravity change for 2011 Mw=9.0 Tohoku earthquake.

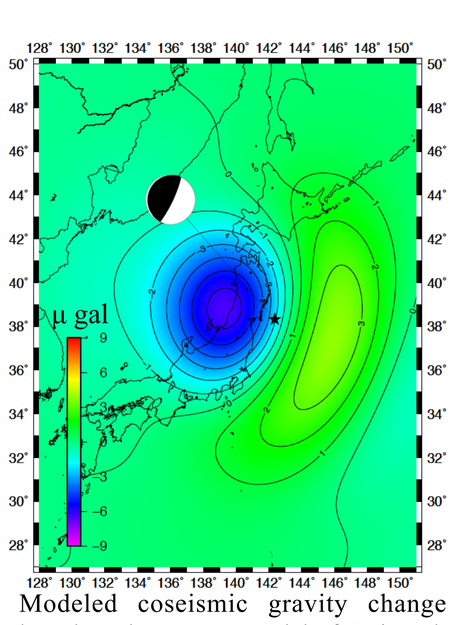

Modeled coseismic gravity change based on the rupture model of Wei et al. [2012]; truncated to degree/order to 60; 300 km Gaussian smooth; consistent with GRACE.

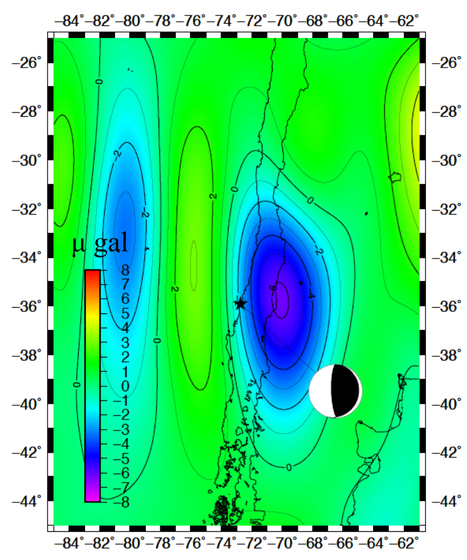

GRACE measured coseismic gravity change for 2010 Mw=8.8 Chile earthquake.

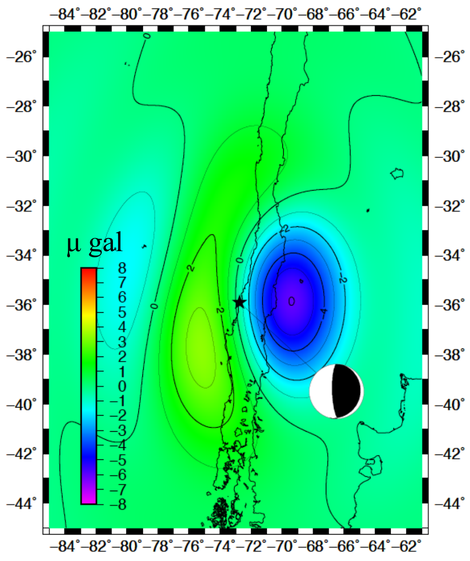

Modeled coseismic gravity change based on the rupture model of Sladen et al; truncated to degree/order to 60; 300 km Gaussian smooth; consistent with GRACE.

Future Work: we will use GRACE measured coseismic gravity change to constrain earthquake rupture process.

SSE at Southcentral Alaska Subduction Zone

A Slow Slip Event (SSE) at the southcentral Alaska subduction zone is identified using GPS measurements. This SSE occurs downdip of the main asperity that ruptured in the 1964 Alaska earthquake, on the same part of the subduction interface as the earlier 1998–2001 SSE. The average slip rate of this SSE is ~4-5 cm/yr, with a cumulative moment magnitude of Mw 7.5. The SSEs occur on a transitional section of the subduction plate interface between the fully locked updip part and the freely slipping deeper part.

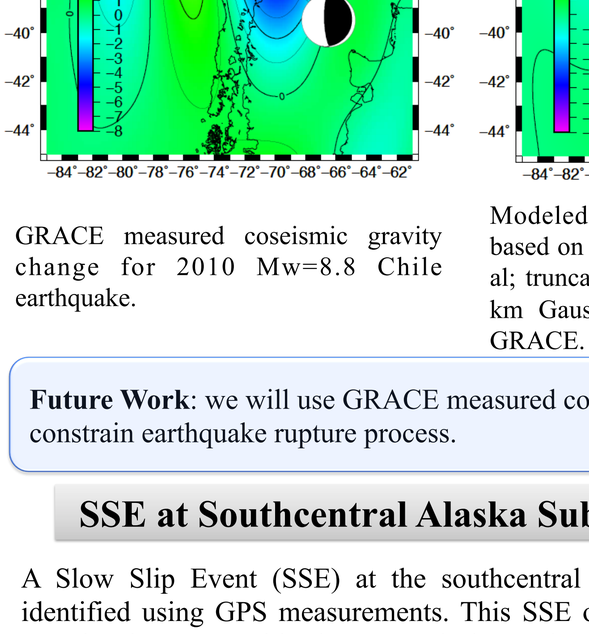

GPS stations used in this study. Red triangles are active volcanoes. The black star denotes the location of Anchorage. The three outlines indicate the previously identified SSEs of Ohta et al. (2006) and Wei et al. (2012).

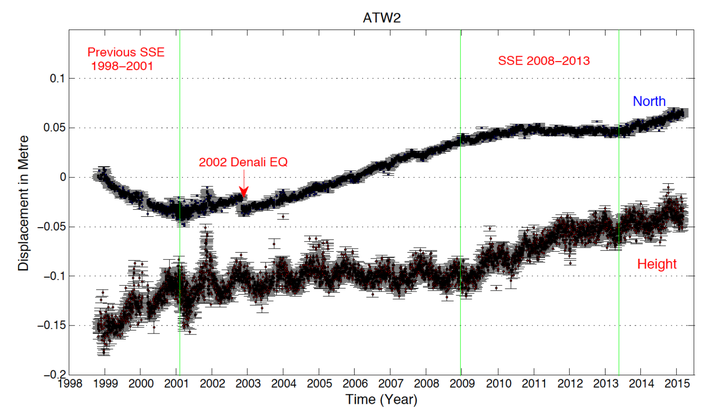

A typical GPS timeseries showing the SSE: north and height components relative to the stable North American plate.

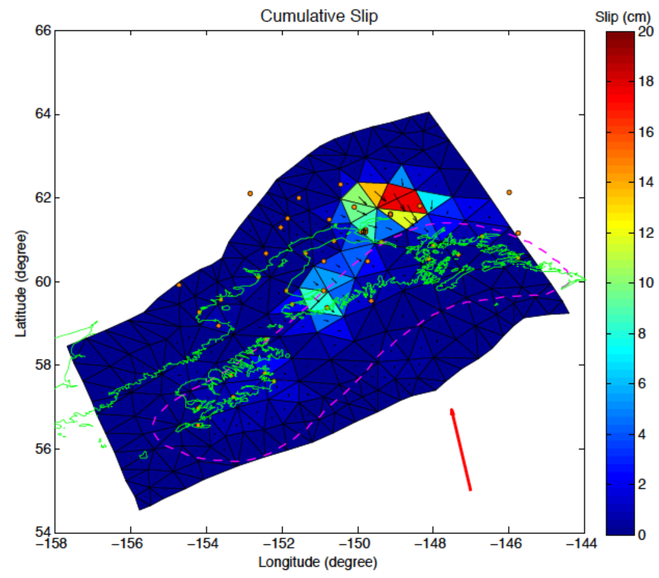

Cumulative slip for the whole SSE from 2008 to 2013. The pink dashed line shows the rupture area of the 1964 Alaska earthquake. The SSE occurs downdip of the main asperity that ruptured in the 1964 earthquake.

Real-time GPS for Tsunami Early Warning

We are using real-time high-rate (1-hz) GPS to quickly determine ground coseismic displacement, and hopefully to provide fast information for tsunami early warning for megathrust earthquakes at subduction zones.

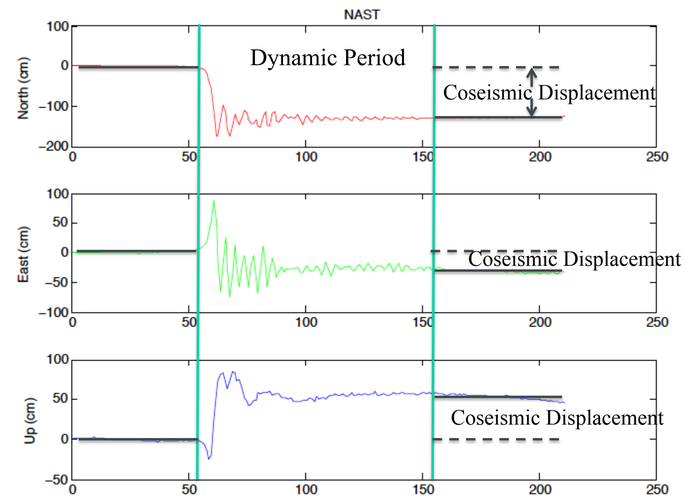

An example of a high-rate GPS measuring the ground displacement of Nepal Mw=7.8 earthquake.

M=6.7 Argentina 2015-02-11 earthquake

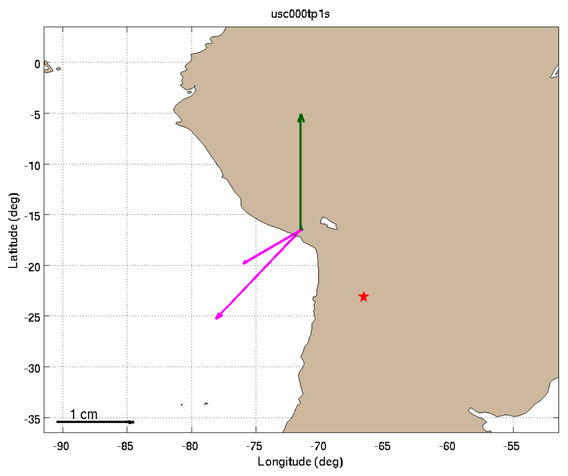

Real-time coseismic displacement determined by our automatic programs for a M=6.7 earthquake in Argentina.

Poster No. EA-20